A new fast multi-domain BEM to model seismic wave propagation and amplification in 3D geological structures

Stéphanie Chaillat, Marc Bonnet, Jean-François Semblat

accepted for publication in *Geophys. J. Int.*

A new fast multi-domain BEM to model seismic wave propagation and amplification in 3D geological structures

S. Chaillat[1,2], M. Bonnet[1], J.F. Semblat[2]

[1] *Ecole Polytechnique, Solid Mechanics Laboratory (UMR CNRS 7649), Palaiseau, France*

[2] *Université Paris-Est, LCPC, MSRGI, Paris, France*

SUMMARY

The analysis of seismic wave propagation and amplification in complex geological structures raises the need for efficient and accurate numerical methods. The solution of the elastodynamic equations using traditional boundary element methods (BEMs) is greatly hindered by the fully-populated nature of the matrix equations arising from the discretization. In a previous study limited to homogeneous media, the present authors have established that the Fast Multipole (FM) method reduces the complexity of a 3-D elastodynamic BEM to $N \log N$ per GMRES iteration and demonstrated its effectiveness on 3-D canyon configurations. In this article, the frequency-domain FM-BEM methodology is extented to 3-D elastic wave propagation in piecewise-homogeneous domains in the form of a FM-accelerated multi-region BE-BE coupling approach. This new method considerably enhances the capability of the BEM for studying the propagation of seismic waves in 3-D alluvial basins of arbitrary geometry embedded in semi-infinite media. Several fully 3-D examples (oblique SV-waves) representative of such configurations validate and demonstrate the capabilities of the multi-domain fast multipole approach. They include comparisons with available (low-frequency) results for various types of incident wavefields, and time-domain results obtained by means of Fourier synthesis.

Key words: Site effects; Computational seismology; Wave propagation

1 INTRODUCTION

Seismic wave propagation in complex geological structures often results in large local amplifications of the ground motion. Seismic wave amplification may be analyzed using either modal approaches (Paolucci 1999; Semblat et al. 2003; Pecker 2005) or direct simulations of wave propagation (Bard & Bouchon 1985; Sánchez-Sesma & Luzón 1995; Bielak et al. 2003; Komatitsch et al. 2004; Semblat et al. 2005). The importance of 2D and 3D realistic simulations is well recognized in the literature (Frankel & Vidale 1992; Paolucci 2002; Makra et al. 2005). Due to rapid and steady increase of available computational capabilities, the simulation of waves in 3D configurations is becoming a very active area of research. Numerical methods proposed so far for the computation of seismic wave propagation in alluvial basins exploit series expansions (Lee 1984), multipolar expansions of wave functions (Sánchez-Sesma 1983), finite

elements (Bielak et al. 2005), finite differences (Saenger et al. 2000; Moczo et al. 2007), spectral elements (Faccioli et al. 1997; Komatitch & Vilotte 1998), or boundary elements (e.g. Guzina & Pak 2001; Dangla et al. 2005), with specific advantages and limitations for each approach. The main advantage of the boundary element method (BEM) is that only the domain boundaries (and possibly interfaces) are discretized, leading to a reduction of the number of degrees of freedom (DOFs), and avoiding cumulative effects of grid dispersion (Ihlenburg & Babuška 1995; Hughes et al. 2008). The BEM is well suited to dealing with unbounded-domain idealizations commonly used in seismology, as exact satisfaction of radiation conditions is built into the formulation (Kupradze 1963; Bonnet 1999). However, the standard BEM leads to fully-populated matrices, which results in high computational costs in CPU time ($O(N^2)$ per iteration using an iterative solver such as GMRES) and memory requirements ($O(N^2)$), where N denotes the number of DOFs of the BEM model. In an effort to overcome such limitations, Bouchon et al. (1995) have proposed, and applied to 2-D layered media, an approach whereby a sparse approximation of the governing matrix is obtained by retaining only the entries with sufficiently high magnitude, later extended to 3-D topographies by Ortiz-Alemán et al. (1998). More generally, the appearance of accelerated boundary element (BE) methodologies, allowing complexities far lower than those of traditional BEMs, has dramatically improved the capabilities of BEMs for many areas of application, largely owing to the rapid development of the Fast Multipole Method (FMM) over the last 10-15 years (see the review article by Nishimura 2002). Such approaches have resulted in considerable solution speedup, memory requirement reduction, and model size increase. The FMM is inherently associated with iterative solvers (usually GMRES), and is known to require $O(N \log N)$ CPU time per iteration for Helmholtz-type equations (Darve 2000; Sylvand 2002; Darve & Havé 2004). To date, only few studies have been devoted to the FMM in elastodynamics (including Fujiwara 2000 for the frequency-domain case, Takahashi et al. 2003 for the time-domain case and Çakir 2006 for a formulation specialized to surface waves), whereas FMMs for the Maxwell equations have been more extensively investigated, see e.g. Lu & Chew (1994); Darve (2000); Sylvand (2002); Gumerov & Duraiswami (2005). In Chaillat et al. (2008), the methodology of Fujiwara (2000) is improved for homogeneous semi-infinite elastic propagation domains by incorporating recent advances of FMM implementations for Maxwell equations (e.g. Darve 2000), allowing to run BEM models of size up to $N = O(10^6)$ on a single-processor PC. The present article aims at extending the formulation of Chaillat et al. (2008) to multi-domain situations, with emphasis on alluvial-basin configurations, by developing a FMM-based BE-BE coupling approach suitable for 3-D piecewise-homogeneous media.

The paper is organized as follows. Classical concepts pertaining the elastodynamic BEM and FMM are reviewed in Section 2. Then, Section 3 presents the BEM formulation for seismic wave propagation in semi-infinite, piecewise-homogeneous media. Next, the FM-based BE-BE coupling strategy is presented in Section 4 together with a detailed discussion of several crucial implementation issues. Several examples representative of seismic wave propagation in 3-D alluvial basins are then presented in Section 5, including comparisons with available (low-frequency) results for various types of incident wavefields, and also time-domain results obtained by means of Fourier synthesis.

2 STANDARD AND FAST MULTIPOLE ACCELERATED BOUNDARY ELEMENT METHOD

This section summarizes existing concepts for single-region elastodynamic BEM and FMM, which will thus provide a foundation for developing a multi-region FM-BEM for modelling complex geological structures such as alluvial basins and other topographical irregularities.

2.1 Single-region boundary element method

Let Ω denote a region of space occupied by an isotropic elastic solid characterized by μ (shear modulus), ν (Poisson's ratio) and ρ (mass density). A time-harmonic motion with circular frequency ω is assumed, and the implicit factor $e^{-i\omega t}$ will be systematically omitted. Assuming the absence of body forces, the displacement $\boldsymbol{u}$ is given at an interior point $\boldsymbol{x} \in \Omega$ by the well-known integral representation formula:

$$u_k(\boldsymbol{x}) = \int_{\partial\Omega} [t_i(\boldsymbol{y}) U_i^k(\boldsymbol{x}, \boldsymbol{y}; \omega) - u_i(\boldsymbol{y}) T_i^k(\boldsymbol{x}, \boldsymbol{y}; \omega)] \, \mathrm{d}S_y \tag{1}$$

where $\boldsymbol{t}$ is the traction vector on the boundary $\partial\Omega$, and $U_i^k(\boldsymbol{x}, \boldsymbol{y}; \omega)$ and $T_i^k(\boldsymbol{x}, \boldsymbol{y}; \omega)$ denote the i-th components of the elastodynamic fundamental solution, i.e. of the displacement and traction, respectively, generated at $\boldsymbol{y} \in \mathbb{R}^3$ by a unit point force applied at $\boldsymbol{x} \in \mathbb{R}^3$ along the direction k (Eringen & Suhubi 1975):

$$\begin{aligned}
U_i^k(\boldsymbol{x}, \boldsymbol{y}; \omega) &= \frac{1}{4\pi k_S^2 \mu} \Big((\delta_{qs}\delta_{ik} - \delta_{qk}\delta_{is}) \frac{\partial}{\partial x_q} \frac{\partial}{\partial y_s} G(|\boldsymbol{y} - \boldsymbol{x}|; k_S) + \frac{\partial}{\partial x_i} \frac{\partial}{\partial y_k} G(|\boldsymbol{y} - \boldsymbol{x}|; k_P) \Big), \\
T_i^k(\boldsymbol{x}, \boldsymbol{y}; \omega) &= \mu \Big[\frac{2\nu}{1 - 2\nu} \delta_{ij}\delta_{k\ell} + \delta_{ik}\delta_{j\ell} + \delta_{jk}\delta_{i\ell} \Big] \frac{\partial}{\partial y_\ell} U_h^k(\boldsymbol{x}, \boldsymbol{y}; \omega) n_j(\boldsymbol{y}), \\
k_S^2 &= \frac{\rho\omega^2}{\mu}, \quad k_P^2 = \frac{1 - 2\nu}{2(1 - \nu)} k_S^2
\end{aligned} \tag{2}$$

in which $G(r; k)$, defined by

$$G(r; k) = \frac{\exp(ikr)}{4\pi r} \tag{3}$$

is the free-space Green's function for the Helmholtz equation with wavenumber k corresponding to either P or S elastic waves, and $\boldsymbol{n}(\boldsymbol{y})$ is the unit normal to $\partial\Omega$ directed outwards of Ω.

When $\boldsymbol{x} \in \partial\Omega$, a singularity occurs at $\boldsymbol{y} = \boldsymbol{x}$. With the help of a well-documented limiting process (e.g. Guiggiani & Gigante 1990), the integral representation (1) yields the integral equation, for $\boldsymbol{x} \in \partial\Omega$:

$$c_{ik}(\boldsymbol{x}) u_i(\boldsymbol{x}) + (\text{P.V.}) \int_{\partial\Omega} u_i(\boldsymbol{y}) T_i^k(\boldsymbol{x}, \boldsymbol{y}; \omega) \mathrm{d}S_y - \int_{\partial\Omega} t_i(\boldsymbol{y}) U_i^k(\boldsymbol{x}, \boldsymbol{y}; \omega) \mathrm{d}S_y = 0 \tag{4}$$

where (P.V.) indicates a Cauchy principal value (CPV) singular integral and the *free-term* $c_{ik}(\boldsymbol{x})$ is equal to $0.5\delta_{ik}$ in the usual case where $\partial\Omega$ is smooth at $\boldsymbol{x}$. Equation (4) may be recast into alternative, equivalent regularized forms which are free of CPV integrals (Bui et al. 1985; Krishnasamy et al. 1992; Pak & Guzina 1999; Dangla et al. 2005).

The numerical solution of boundary integral equation (4) is based on a boundary element (BE) discretization of the surface $\partial\Omega$ and boundary traces (u, t), leading to the system (Bonnet 1999):

$$[H]\{u\} + [G]\{t\} = 0, \tag{5}$$

where $[H]$ and $[G]$ are fully populated, nonsymmetric, matrices and vectors $\{u\}$, $\{t\}$ gather the displacement and traction degrees of freedom (DOFs). In this work, linear three-noded triangular boundary elements are used, together with a piecewise-linear continuous (i.e. isoparametric) interpolation for the displacements and a piecewise-constant interpolation of tractions. Upon introduction of boundary conditions, the matrix equation (5) is recast in the form:

$$[K]\{v\} = \{f\}, \tag{6}$$

where the N-vector $\{v\}$ collects the unknown degrees of freedom (DOFs), while the $N \times N$

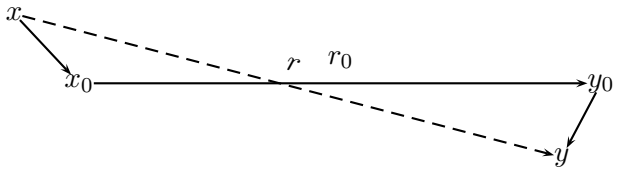

Figure 1. Decomposition of the position vector: notations.

matrix of influence coefficients $[K]$ contains the columns of $[H]$ and $[G]$ associated with the unknown components.

BEM matrix equations such as (6) are here solved iteratively using the GMRES algorithm (Saad & Schultz 1986). The influence matrix $[K]$ is fully-populated. With reference to (6), each GMRES iteration requires one evaluation of $[K]\{v\}$ for given $\{v\}$, a task requiring a computing time of order $O(N^2)$ regardless of whether $[K]$ is stored or $[K]\{v\}$ is evaluated by means of standard BEM numerical integration procedures. To lower this $O(N^2)$ complexity, which is unacceptable for large BEM models, fast BEM solutions techniques such as the Fast Multipole Method (FMM) must be employed.

2.2 Fast Multipole Method: principle

The goal of the FMM is to speed up the matrix-vector product computation required for each iteration of the iterative solver applied to the BEM-discretized equations. Moreover, the governing BEM matrix is never explicitly formed, which leads to a storage requirement well below the $O(N^2)$ memory required for holding it. Substantial savings in both CPU time and memory are thus achieved.

In general terms, the FMM exploits a reformulation of the fundamental solutions in terms of products of functions of $\boldsymbol{x}$ and of $\boldsymbol{y}$, so that (unlike in the traditional BEM) integrations with respect to $\boldsymbol{y}$ can be reused when the collocation point $\boldsymbol{x}$ is changed. On decomposing the position vector $\boldsymbol{r} = \boldsymbol{y} - \boldsymbol{x}$ into $\boldsymbol{r} = (\boldsymbol{y} - \boldsymbol{y_0}) + \boldsymbol{r_0} - (\boldsymbol{x} - \boldsymbol{x_0})$, where $\boldsymbol{x_0}$ and $\boldsymbol{y_0}$ are two poles and $\boldsymbol{r_0} = \boldsymbol{y_0} - \boldsymbol{x_0}$ (Fig. 1) and invoking the Gegenbauer addition theorem, the Helmholtz Green's function is written as (Epton & Dembart 1995; Darve 2000):

$$G(|\boldsymbol{r}|,k) = \lim_{L\to+\infty} \int_{\hat{\boldsymbol{s}}\in S} e^{ik\hat{\boldsymbol{s}}.(\boldsymbol{y}-\boldsymbol{y_0})} \mathcal{G}_L(\hat{\boldsymbol{s}};\boldsymbol{r_0};k) e^{-ik\hat{\boldsymbol{s}}.(\boldsymbol{x}-\boldsymbol{x_0})} d\hat{\boldsymbol{s}}, \tag{7}$$

where S is the unit sphere of $\mathbb{R}^3$ and the *transfer function* $\mathcal{G}_L(\hat{\boldsymbol{s}};\boldsymbol{r_0};k)$ is defined in terms of the Legendre polynomials P_p and the spherical Hankel functions of the first kind $h_p^{(1)}$ by:

$$\mathcal{G}_L(\hat{\boldsymbol{s}};\boldsymbol{r_0};k) = \frac{ik}{16\pi^2} \sum_{0\le p\le L} (2p+1) i^p h_p^{(1)}(k|\boldsymbol{r_0}|) P_p\big(cos(\hat{\boldsymbol{s}},\boldsymbol{r_0})\big) \tag{8}$$

Then, the elastodynamic fundamental solution (2) is easily seen to admit representations of the form (7) with $\mathcal{G}_L$ replaced with suitably-defined (tensor) transfer functions (Chaillat et al. 2008).

A 3D cubic grid of linear spacing d embedding the whole boundary $\partial\Omega$ is then introduced. The FMM basically consists in using decomposition (7), with the poles $\boldsymbol{x_0}$ and $\boldsymbol{y_0}$ being chosen as the cell centers, whenever $\boldsymbol{x}$ and $\boldsymbol{y}$ belong to *non-adjacent* cubic cells. The treatment of such "FM" contributions exploits the multipole expansions of the fundamental solutions (2), truncated at a finite L and in a manner suggested by their multiplicative form. When $\boldsymbol{x}$ and $\boldsymbol{y}$ belong to adjacent cells, traditional BEM evaluation methods based on expressions (2) and (3) are used. To improve further the computational efficiency of the FM-BEM, standard

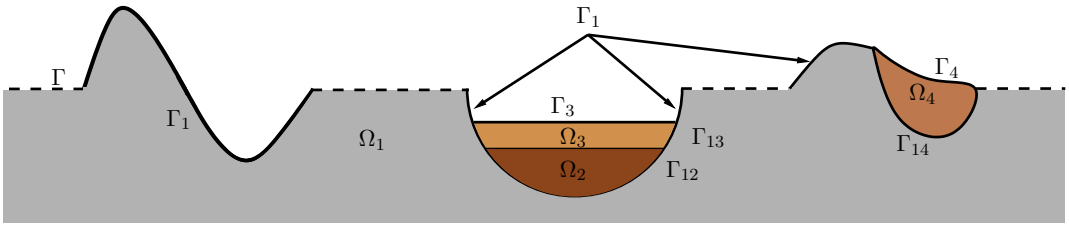

Figure 2. Propagation of seismic waves in complex geological structures (alluvial deposits, basins): various geometries and related notations.

(i.e. non-FMM) calculations must be confined to the smallest possible spatial regions while retaining the advantage of clustering the computation of influence terms into non-adjacent large groups whenever possible. This is achieved by recursively subdividing cubic cells into eight smaller cubic cells. New pairs of non-adjacent smaller cells, to which multipole expansions are applicable, are thus obtained from the subdivision of pairs of adjacent cells. The cell-subdivision approach is systematized by means of an oct-tree structure of cells. At each level ℓ, the linear cell size is denoted d^ℓ. The level $\ell = 0$, composed of only one cubic cell containing the whole surface $\partial\Omega$, is the tree root. The subdivision process is further repeated until the finest level $\ell = \bar{\ell}$, implicitly defined by a preset subdivision-stopping criterion ($d^{\bar{\ell}} \geq d^{\min}$), is reached. Level-$\bar{\ell}$ cells are usually termed leaf cells. This is the essence of the multi-level FMM, whose theoretical complexity is $O(N \log N)$ per GMRES iteration both for CPU time and memory (see Chaillat et al. 2008 for further details on the method and its implementation for single-domain elastodynamic problems).

3 CONTINUOUS BEM FORMULATIONS FOR SEISMIC WAVE PROPAGATION

In this section, the continuous BIE formulations for the propagation of seismic waves in complex geological structures (topographic irregularities, alluvial basins, ...) are presented. Such formulations, and their present implementation based on the multi-domain FM-accelerated BEM (Section 4), are geared towards geometrical configurations involving a semi-infinite homogeneous reference medium with topographic irregularities and alluvial deposits (henceforth generically referred to as irregularities, Fig. 2). Although integral equation formulations for elastic-wave scattering in such configurations are not novel in their principle, they are rarely expounded in detail, hence our choice to devote this section to their comprehensive presentation for general geological configurations.

In the following, Ω_F denotes the free half-space $\{\boldsymbol{x} = (x_1, x_2, x_3) \mid x_3 < 0\}$ bounded by the infinite traction-free surface $\Gamma_F = \{\boldsymbol{x} \mid x_3 = 0\}$. Configurations treated in this article are perturbations of the free half-space Ω_F, where irregularities occur only in a region of finite size. For such configurations, the displacement vector $\boldsymbol{u}$ is split into:

$$\boldsymbol{u} = \boldsymbol{u}^F + \boldsymbol{u}^S \tag{9}$$

where $\boldsymbol{u}^F$ characterizes the free-field, a known seismic wave in the reference free half-space Ω_F composed of the incident waves and those reflected from the planar free surface Γ_F, so that $\boldsymbol{t}^F = 0$ on Γ_F. The scattered displacement $\boldsymbol{u}^S$ then arises due to the presence of irregularities. On any non-planar part of the free surface, one has $t^S + t^F = 0$.

In the following, shorthand notations U_i^k and T_i^k are used instead of $U_i^k(\boldsymbol{x}, \boldsymbol{y}; \omega)$ and $T_i^k(\boldsymbol{x}, \boldsymbol{y}; \omega)$ for expository convenience.

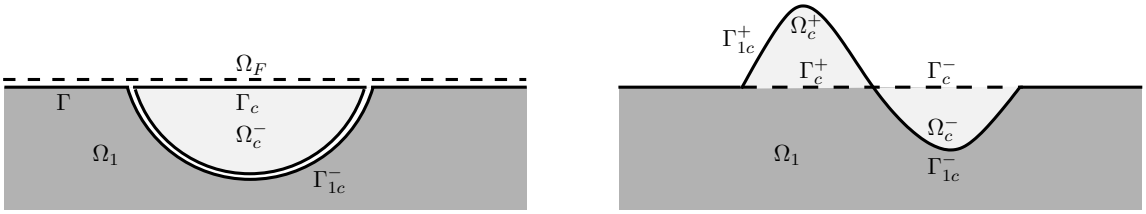

Figure 3. Definition of the complementary domain $\Omega_c = \Omega_c^+ \cup \Omega_c^-$ for the determination of the total field in Ω_1.

3.1 Diffraction of incident waves by a topographic irregularity

The diffraction of an incident wave by topographic irregularities (e.g. a canyon), defined as deviations of the free surface from the infinite plane Γ_F, is first considered. Such configurations consist of a homogeneous semi-infinite medium occupying the domain Ω_1 situated below the infinite traction-free surface $\partial\Omega_1 = \Gamma \cup \Gamma_1$, where the bounded (and possibly non-connected) surface Γ_1 defines the topographic irregularities and $\Gamma = \partial\Omega_1 \cap \Gamma_F$ is the (unbounded) planar component of the free surface (Fig. 2). Because $\boldsymbol{u^S}$ and $\boldsymbol{t^S}$ satisfy the radiation condition at infinity (Eringen & Suhubi 1975; Madyarov & Guzina 2006), it follows from (4) that the scattered field satisfies:

$$c_{ik}(\boldsymbol{x})u_i^S(\boldsymbol{x}) + \int_{\partial\Omega_1} \Big(u_i^S(\boldsymbol{y})T_i^k - t_i^S(\boldsymbol{y})U_i^k \Big) dS_y = 0, \ \forall \boldsymbol{x} \in \partial\Omega_1 \tag{10}$$

Incorporating the free-surface conditions $\boldsymbol{t}^S = \boldsymbol{0}$ (on Γ) and $\boldsymbol{t}^S + \boldsymbol{t}^F = \boldsymbol{0}$ (on Γ_1), equation (10) becomes:

$$c_{ik}(\boldsymbol{x})u_i^S(\boldsymbol{x}) + \int_{\partial\Omega_1} u_i^S(\boldsymbol{y})T_i^k dS_y = -\int_{\Gamma_1} t_i^F(\boldsymbol{y})U_i^k dS_y, \ \forall \boldsymbol{x} \in \partial\Omega_1 \tag{11}$$

The problem may thus be solved in terms of scattered wavefield only. To recover the total displacement, one may simply invoke the decomposition (9) in a post-processing step. However, for dealing next with the multi-domain problems arising when irregularities include deposits, the transmission conditions at the subdomain interfaces are best formulated in terms of total fields $\boldsymbol{u}, \boldsymbol{t}$. Anticipating this need, it is therefore useful to establish the counterpart of integral equation (11) formulated in terms of total fields.

To obtain the equation satisfied in Ω_1 by the total field, we consider the (bounded) complementary domain $\Omega_c = \Omega_c^+ \cup \Omega_c^-$ of Ω_1 relative to the half-space Ω_F, where $\Omega_c^- = \Omega_F \backslash (\Omega \cup \partial\Omega)$ and $\Omega_c^+ = \Omega \backslash (\Omega_F \cup \Gamma_F)$ are the parts of Ω_c situated below and above Γ_F, respectively (Fig. 3). In Ω_c^+, the displacements $\boldsymbol{u}^F(\boldsymbol{x})$ and tractions $\boldsymbol{t}^F(\boldsymbol{x})$ associated with the free-field satisfy the following equation:

$$c_{ik}^{c+}(\boldsymbol{x})u_i^F(\boldsymbol{x}) + \int_{\Gamma_{c1}^+ \cup \Gamma_c^+} u_i^F(\boldsymbol{y})T_i^k dS_y - \int_{\Gamma_{c1}^+} t_i^F(\boldsymbol{y})U_i^k dS_y = 0, \ \forall \boldsymbol{x} \in \partial\Omega_1 \tag{12}$$

where c_{ik}^{c+} denotes the free-term relative to Ω_c^+, having set $\Gamma_c^+ = \partial\Omega_c^+ \cap \Gamma_F$ and $\Gamma_{c1}^+ = \partial\Omega_c^+ \cap \Gamma_1$, and in which the free-surface condition is incorporated. Using similar notation, the corresponding integral equation associated with the free field in Ω_c^- reads:

$$c_{ik}^{c-}(\boldsymbol{x})u_i^F(\boldsymbol{x}) + \int_{\Gamma_{c1}^- \cup \Gamma_c^-} u_i^F(\boldsymbol{y})T_i^k dS_y - \int_{\Gamma_{c1}^-} t_i^F(\boldsymbol{y})U_i^k dS_y = 0, \ \forall \boldsymbol{x} \in \partial\Omega_1 \tag{13}$$

where c_{ik}^{c-} denotes the free-term relative to Ω_c^-.

On setting $\Gamma_1 = \Gamma_{1c}^+ \cup \Gamma_{c1}^-$ in (10), performing the combination (10) + (12) - (13) and

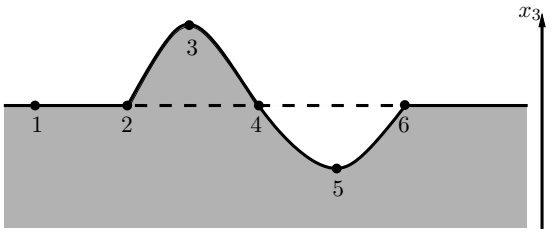

Figure 4. Diffraction of a wave by a canyon: various cases for the location of $\boldsymbol{x} \in \partial\Omega_1$ considered for the computation of the free term.

noting that pairs Γ_{c1}^-, Γ_{1c}^- and Γ_c^+, Γ_c define identical surfaces with opposite normals, one obtains:

$$\begin{aligned} &c_{ik}(\boldsymbol{x})u_i^S(\boldsymbol{x}) - c_{ik}^{c-}(\boldsymbol{x})u_i^F(\boldsymbol{x}) + c_{ik}^{c+}(\boldsymbol{x})u_i^F(\boldsymbol{x}) + \int_{\Gamma_{1c}^+\cup\Gamma_{1c}^-} \Big(u_i^S(\boldsymbol{y}) + u_i^F(\boldsymbol{y})\Big) T_i^k dS_y \\ &+ \int_\Gamma u_i^S(\boldsymbol{y}) T_i^k dS_y - \int_{\Gamma_c^+\cup\Gamma_c^-} u_i^F(\boldsymbol{y}) T_i^k dS_y - \int_{\Gamma_{1c}^+\cup\Gamma_{1c}^-} \Big(t_i^S(\boldsymbol{y}) + t_i^F(\boldsymbol{y})\Big) U_i^k dS_y = 0, \ \forall \boldsymbol{x} \in \partial\Omega_1 \end{aligned} \tag{14}$$

which is reformulated in terms of the total field by invoking decomposition (9):

$$\begin{aligned} c_{ik}(\boldsymbol{x})u_i(\boldsymbol{x}) \quad &+ \int_{\Gamma_{1c}^+\cup\Gamma_{1c}^-} u_i(\boldsymbol{y}) T_i^k dS_y + \int_\Gamma u_i^S(\boldsymbol{y}) T_i^k dS_y - \int_{\Gamma_{1c}^+\cup\Gamma_{1c}^-} t_i(\boldsymbol{y}) U_i^k dS_y \\ &= c_{ik}^F(\boldsymbol{x})u_i^F(\boldsymbol{x}) + \int_{\Gamma_c^+\cup\Gamma_c^-} u_i^F(\boldsymbol{y}) T_i^k dS_y, \ \forall \boldsymbol{x} \in \partial\Omega_1 \end{aligned} \tag{15}$$

having set $c_{ik}^F(\boldsymbol{x}) = c_{ik}^{c-}(\boldsymbol{x}) - c_{ik}^{c+}(\boldsymbol{x}) + c_{ik}(\boldsymbol{x})$. To evaluate $c_{ik}^F(\boldsymbol{x})$, six cases need to be considered for the location of $\boldsymbol{x}$ on $\partial\Omega_1$, as indicated on Fig. 4:

case 1:	$c_{ik}(\boldsymbol{x}) = \frac{1}{2}\delta_{ik}$,	$c_{ik}^{c-}(\boldsymbol{x}) = c_{ik}^{c+}(\boldsymbol{x}) = 0$,
case 2:	$-c_{ik}^{c+}(\boldsymbol{x}) + c_{ik}(\boldsymbol{x}) = \frac{1}{2}\delta_{ik}$,	$c_{ik}^{c-}(\boldsymbol{x}) = 0$,
case 3:	$-c_{ik}^{c+}(\boldsymbol{x}) + c_{ik}(\boldsymbol{x}) = 0$,	$c_{ik}^{c-}(\boldsymbol{x}) = 0$,
case 4:	$c_{ik}^{c-}(\boldsymbol{x}) - c_{ik}^{c+}(\boldsymbol{x}) + c_{ik}(\boldsymbol{x}) = \frac{1}{2}\delta_{ik}$,	
case 5:	$c_{ik}^{c-}(\boldsymbol{x}) + c_{ik}(\boldsymbol{x}) = \delta_{ik}$,	$c_{ik}^{c+}(\boldsymbol{x}) = 0$,
case 6:	$c_{ik}^{c-}(\boldsymbol{x}) + c_{ik}(\boldsymbol{x}) = \frac{1}{2}\delta_{ik}$,	$c_{ik}^{c+}(\boldsymbol{x}) = 0$,

It follows that the combination $c_{ik}^F(\boldsymbol{x})$ has just three possible values, depending on the position of $\boldsymbol{x}$ relative to Γ_F:

$$c_{ik}^F(\boldsymbol{x}) = 0 \ (x_3 > 0), \quad c_{ik}^F(\boldsymbol{x}) = \frac{1}{2}\delta_{ik} \ (x_3 = 0), \quad c_{ik}^F(\boldsymbol{x}) = \delta_{ik} \ (x_3 < 0), \tag{16}$$

i.e. $c_{ik}^F(\boldsymbol{x})$ is identical to the usual free-term relative to the half-space Ω_F without irregularity. Finally, it is necessary for practical implementation purposes to introduce a truncated version $\Gamma(D)$ of the free surface Γ, here bounded by a circle of radius D, which will support the BE discretization. The integral in the left-hand side of eq. (17) below is known to be convergent in the limit $\Gamma(D) \to \Gamma$, hence so is the right-hand side:

$$\int_{\Gamma(D)} u_i^S(\boldsymbol{y}) T_i^k dS_y = \int_{\Gamma(D)} u_i(\boldsymbol{y}) T_i^k dS_y - \int_{\Gamma(D)} u_i^F(\boldsymbol{y}) T_i^k dS_y \tag{17}$$

Incorporing (17) into (15), it follows:

$$c_{ik}(\boldsymbol{x})u_i(\boldsymbol{x}) + \int_{\Gamma_1\cup\Gamma(D)} u_i(\boldsymbol{y})T_i^k dS_y - \int_{\Gamma_1} t_i(\boldsymbol{y})U_i^k dS_y = c_{ik}^F(\boldsymbol{x})u_i^F(\boldsymbol{x}) + \int_{\Gamma_F(D)} u_i^F(\boldsymbol{y})T_i^k dS_y, \quad \forall \boldsymbol{x} \in \partial\Omega_1 \quad (18)$$

where $c_{ik}^F(\boldsymbol{x})$ is defined by eq. (16), $\Gamma_F(D)$ is the truncated version of Γ_F, and strict equality occurs only in the limiting case $D \to +\infty$.

3.2 Propagation of incident waves in alluvial basins

Of primary interest in this article is, the propagation of an incident wave in an alluvial basin, leading to a multi-domain BEM formulation. Accordingly, let Ω_1 denote a semi-infinite homogeneous medium possibly featuring a topographic irregularity of finite spatial extension. Other materials (e.g. sediments) occupy $(n-1)$ bounded regions Ω_i $(2 \leq i \leq n)$ such that $\Omega_1 \cap \Omega_i = \emptyset$ (Fig. 2).

In the following, $\Gamma = \partial\Omega_1 \cap \Gamma_F$ denotes the (unbounded) portion of planar free surface intercepted by Ω_1, Γ_i $(i = 1, \ldots, n)$ denotes the (bounded) portion of $\partial\Omega_i$ situated on the free surface but not included in Γ (so that the disjoint union $\Gamma \cup \Gamma_1 \cup \ldots \cup \Gamma_n$ constitutes the free surface) and Γ_{ij} denotes the interface between Ω_i and Ω_j so that one has $\partial\Omega_1 = \Gamma \cup \Gamma_1 \cup \Gamma_{12} \cup \ldots \cup \Gamma_{1n}$ and $\partial\Omega_i = \Gamma_i \cup \Gamma_{i1} \cup \ldots \cup \Gamma_{in}$ $(i \geq 2)$. For subregions Ω_i, Ω_j that do not share interfaces, one has of course $\Gamma_{ij} = \emptyset$. $\boldsymbol{t^{ij}}$ denotes the traction vector on Γ_{ij}, conventionally defined in terms of the normal $\boldsymbol{n}_{ij}$ oriented from Ω_i to Ω_j (Fig. 5); hence $\boldsymbol{t}_{ij} = -\boldsymbol{t}_{ji}$ with this convention. The governing equation for the total field in Ω_1 is (18) where Γ_1 is replaced with $\Gamma_1 \cup \Gamma_{12} \cup \ldots \cup \Gamma_{1n}$, i.e.:

$$c_{ik}(\boldsymbol{x})u_i(\boldsymbol{x}) + \int_{\Gamma_1\cup\Gamma(D)} u_i^1(\boldsymbol{y})T_i^{k(1)} dS_y + \sum_{m=2}^{n} \Big(\int_{\Gamma_{1m}} u_i^{1m}(\boldsymbol{y})T_i^{k(1)} dS_y \Big) - \int_{\Gamma_1} t_i^1(\boldsymbol{y})U_i^{k(1)} dS_y$$
$$- \sum_{m=2}^{n} \Big(\int_{\Gamma_{1m}} t_i^{1m}(\boldsymbol{y})U_i^{k(1)} dS_y \Big) = c_{ik}^F(\boldsymbol{x})u_i^F(\boldsymbol{x}) + \int_{\Gamma_F(D)} u_i^F(\boldsymbol{y})T_i^{k(1)} dS_y, \ \forall \boldsymbol{x} \in \partial\Omega_1 \quad (19)$$

where $U_i^{k(1)}$ and $T_i^{k(1)}$ are the fundamental solutions defined in terms of the material parameters of Ω_1. In the free-term of (19), $u_i(\boldsymbol{x})$ stands for either $u_i^1(\boldsymbol{x})$ or $u_i^{1m}(\boldsymbol{x})$, according to whether the collocation point $\boldsymbol{x}$ lies on Γ_1 or Γ_{1m}.

The total field in subdomain Ω_ℓ $(\ell > 1)$ is governed by the integral equation:

$$c_{ik}(\boldsymbol{x})u_i(\boldsymbol{x}) + \int_{\Gamma_\ell} u_i^\ell(\boldsymbol{y})T_i^{k(\ell)} + \sum_{\substack{m\geq 1 \\ m\neq\ell}} \int_{\Gamma_{\ell m}} \Big(u_i^{\ell m}(\boldsymbol{y})T_i^{k(\ell)} - t_i^{\ell m}(\boldsymbol{y})U_i^{k(\ell)} \Big) dS_y = 0,$$
$$\forall \boldsymbol{x} \in \partial\Omega_\ell \ (2 \leq \ell \leq n) \quad (20)$$

where $U_i^{k(\ell)}$ and $T_i^{k(\ell)}$ denote the fundamental solutions defined in terms of the constitutive parameters of Ω_ℓ, the free surface condition on Γ_ℓ has been taken into account, and $u_i(\boldsymbol{x})$ stands for either $u_i^\ell(\boldsymbol{x})$ or $u_i^{\ell m}(\boldsymbol{x})$ according to whether $\boldsymbol{x} \in \Gamma_\ell$ or $\boldsymbol{x} \in \Gamma_{\ell m}$. In addition, invoking transmission conditions

$$\boldsymbol{u}^{\ell m} = \boldsymbol{u}^{m\ell}; \ \boldsymbol{t}^{\ell m} = -\boldsymbol{t}^{m\ell}, \quad (21)$$

which express perfect bonding at interfaces, allows to eliminate $\boldsymbol{u}^{m\ell}$, $\boldsymbol{t}^{m\ell}$ and retain $\boldsymbol{u}^{\ell m}$, $\boldsymbol{t}^{\ell m}$

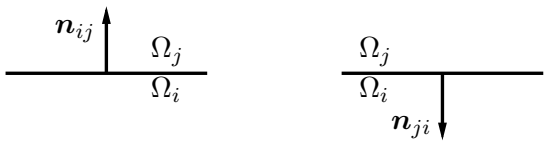

Figure 5. Definition of the traction unknowns.

($\ell < m$) as the interfacial unknowns. Equations (20) thus become:

$$\begin{aligned} &c_{ik}(\boldsymbol{x})u_i(\boldsymbol{x}) + \int_{\Gamma_\ell} u_i^\ell(\boldsymbol{y})T_i^{k(\ell)}dS_y + \sum_{m=2}^{\ell-1}\int_{\Gamma_{\ell m}} \Big(u_i^{m\ell}(\boldsymbol{y})T_i^{k(\ell)} + t_i^{m\ell}(\boldsymbol{y})U_i^{k(\ell)}\Big)dS_y \\ &+ \sum_{m=\ell+1}^{n}\int_{\Gamma_{\ell m}} \Big(u_i^{\ell m}(\boldsymbol{y})T_i^{k(\ell)} - t_i^{\ell m}(\boldsymbol{y})U_i^{k(\ell)}\Big)dS_y = 0,\ \forall \boldsymbol{x} \in \partial\Omega_\ell,\ (2 \le \ell \le n) \end{aligned} \tag{22}$$

The coupled BE-BE formulation to be presented next will then be based on combining discrete versions of equation (19) and equations (22) written for each subregion Ω_ℓ ($\ell \ge 2$). It is similar to the one used for two subdomains in Fujiwara (2000), but more general as (i) it is applicable to an arbitrary number of subdomains and (ii) it accomodates irregularities going *above* or *through* the free surface (Fig. 4).

4 NUMERICAL IMPLEMENTATION OF FM-ACCELERATED BE-BE COUPLING

4.1 BE-BE coupling strategy

The present discrete coupled BE-BE formulation is based on three-noded triangular boundary elements, piecewise-linear interpolation of displacements, and piecewise-constant interpolation of tractions. Since only Neumann or transmission boundary conditions are considered here, the displacement is unknown at all mesh nodes, while the traction is unknown on each interfacial element. The chosen "element-based" traction interpolation permits traction discontinuities across edges. This is particularly convenient when the latter are made of "triple points" shared by three (or more) subregions, whereas "node-based" traction modelling would entail cumbersome adjustments due to the multiplicity of tractions from adjacent faces at such points. The proposed BE-BE coupling formulation is designed so as to invoke single-region FM-BEM computations in "black-box" fashion (here using the elastodynamic FM-BEM formulation presented in Chaillat et al. 2008). To this end, a boundary integral equation is formulated for each subregion Ω_i (with material properties assumed homogeneous in each Ω_i) following Sec. 3.2, and discrete BE equations are generated by using (i) all displacement nodes and (ii) all interfacial element centers as collocation points ((i) and (ii) will subsequently be referred to as "nodal collocation" and "element collocation", respectively). Each subregion is treated separately, using a separate octree for FMM computations. The matrix-vector products arising in each of these integral equations can thus be evaluated using the FM-BEM procedure for homogeneous media presented in Chaillat et al. (2008). The resulting algorithm is schematically described in Fig. 6.

The BE-BE coupling does not, however, just consist of concatenating all single-region BE equations into one global system of equations, as the latter would be overdetermined as a result. One way to ensure that the present BE-BE coupling defines a square global system of equations consists in judiciously defining linear combinations of BE equations generated at the subregion level, a treatment that can be done externally to the FM-BEM computations.

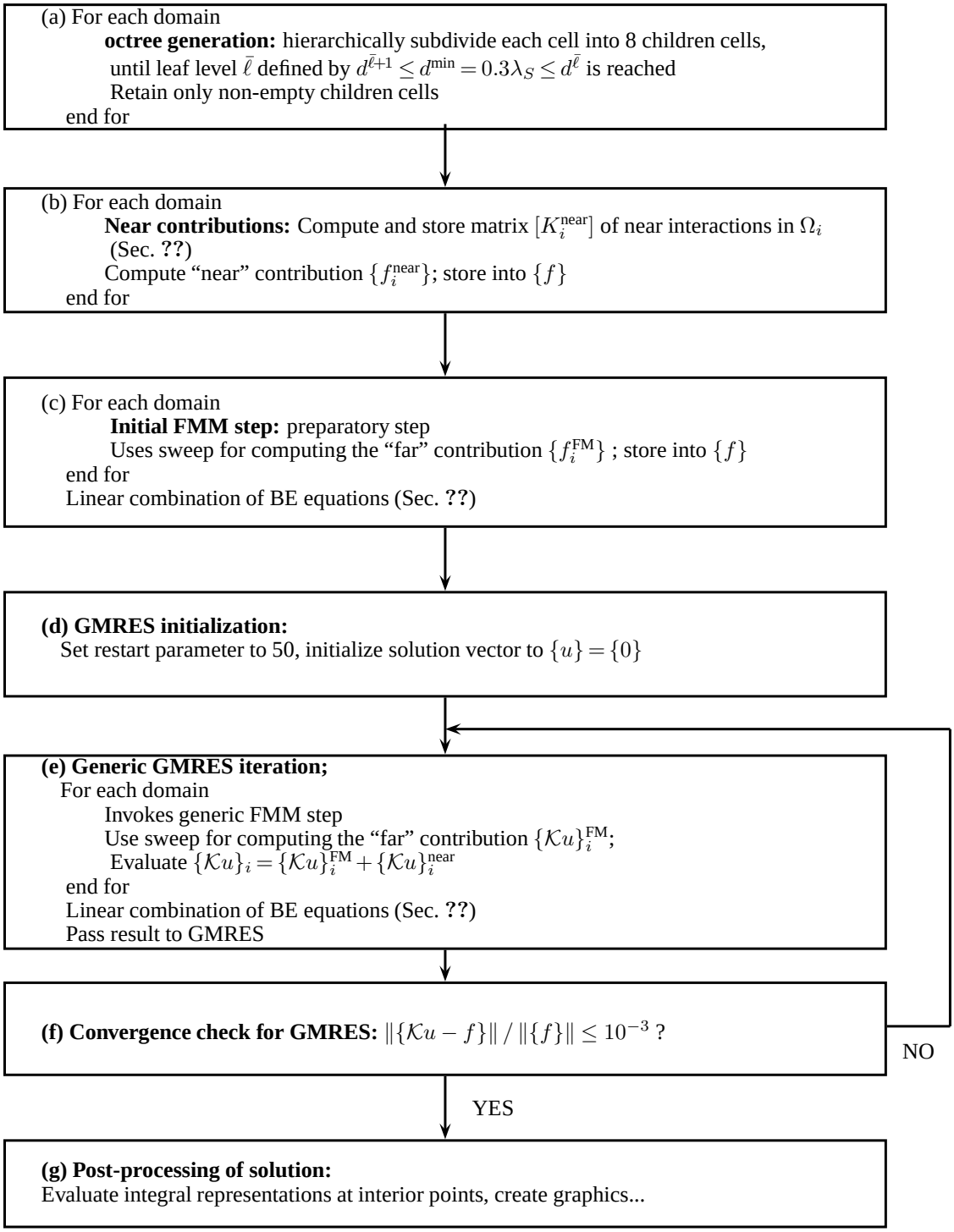

Figure 6. Elastodynamic multi-domain multi-level FM-BEM: schematic description of overall algorithm.

Specifically, linear combinations of BE equations arising from collocation at (a) interfacial element centers relative to either subregion adjacent to that element, and (b) displacement nodes shared by more than one subregion, are defined. This approach ensures that the number of final global BE equations matches the number of unknown BE DOFs, i.e. is square. In

[t]

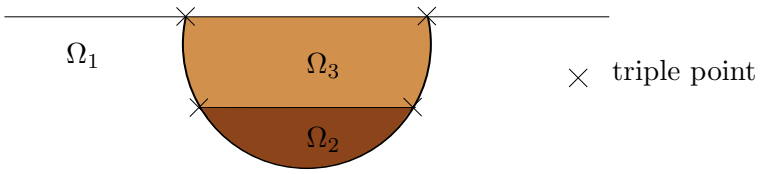

Figure 7. Two-layered basin: definition of triple points.

particular, using this method, multiple displacement nodes are easily handled (see Fig. 7 for an example of triple points in the case of a two-layered basin).

For the sake of definiteness, the above-outlined procedure is now going to be detailed for a representative configuration, namely the case of a two-layered basin (Fig. 7). First, integral equation (19) for the subdomain Ω_1 gives rise to the following set of equations:

$$H_1^1\boldsymbol{u}^1 + H_{12}^1\boldsymbol{u}^{12} + H_{13}^1\boldsymbol{u}^{13} + H_{123}^1\boldsymbol{u}^{123} - G_{12}^1\boldsymbol{t}^{12} - G_{13}^1\boldsymbol{t}^{13} - f^1 = 0, \tag{23a}$$

$$H_1^{12}\boldsymbol{u}^1 + H_{12}^{12}\boldsymbol{u}^{12} + H_{13}^{12}\boldsymbol{u}^{13} + H_{123}^{12}\boldsymbol{u}^{123} - G_{12}^{12}\boldsymbol{t}^{12} - G_{13}^{12}\boldsymbol{t}^{13} - f^{12} = 0, \tag{23b}$$

$$H_1^{13}\boldsymbol{u}^1 + H_{12}^{13}\boldsymbol{u}^{12} + H_{13}^{13}\boldsymbol{u}^{13} + H_{123}^{13}\boldsymbol{u}^{123} - G_{12}^{13}\boldsymbol{t}^{12} - G_{13}^{13}\boldsymbol{t}^{13} - f^{13} = 0, \tag{23c}$$

$$H_1^{123}\boldsymbol{u}^1 + H_{12}^{123}\boldsymbol{u}^{12} + H_{13}^{123}\boldsymbol{u}^{13} + H_{123}^{123}\boldsymbol{u}^{123} - G_{12}^{123}\boldsymbol{t}^{12} - G_{13}^{123}\boldsymbol{t}^{13} - f^{123} = 0, \tag{23d}$$

$$\bar{H}_1^{12}\boldsymbol{u}^1 + \bar{H}_{12}^{12}\boldsymbol{u}^{12} + \bar{H}_{13}^{12}\boldsymbol{u}^{13} + \bar{H}_{123}^{12}\boldsymbol{u}^{123} - \bar{G}_{12}^{12}\boldsymbol{t}^{12} - \bar{G}_{13}^{12}\boldsymbol{t}^{13} - \bar{f}^{12} = 0, \tag{23e}$$

$$\bar{H}_1^{13}\boldsymbol{u}^1 + \bar{H}_{12}^{13}\boldsymbol{u}^{12} + \bar{H}_{13}^{13}\boldsymbol{u}^{13} + \bar{H}_{123}^{13}\boldsymbol{u}^{123} - \bar{G}_{12}^{13}\boldsymbol{t}^{12} - \bar{G}_{13}^{13}\boldsymbol{t}^{13} - \bar{f}^{13} = 0. \tag{23f}$$

In equations (23a-d), notations H_β^γ (for generic single or multiple indices γ, β, e.g. $\gamma = 12$, $\beta = 123$) refer to the submatrices arising from BE discretization of the integral operator

$$\boldsymbol{c}(\boldsymbol{x}).\boldsymbol{u}(\boldsymbol{x}) + \int_{\partial\Omega_m} \boldsymbol{T}^{(m)}(\boldsymbol{x},\boldsymbol{y},\omega).\boldsymbol{u}(\boldsymbol{y})dS_y, \tag{24}$$

upon performing nodal collocation on Γ_γ and retaining only the columns corresponding to u^β. Following the same idea, submatrices $\bar{H}_\beta^\gamma$ are defined in terms of element collocation on Γ_γ instead of nodal collocation, and submatrices G_β^γ, $\bar{G}_\beta^\gamma$ similarly arise from the integral operator

$$\int_{\partial\Omega_m} \boldsymbol{U}^{(m)}(\boldsymbol{x},\boldsymbol{y},\omega).\boldsymbol{t}(\boldsymbol{y})dS_y, \tag{25}$$

Note that the subregion number m is encoded as the first index in γ. For instance, $\gamma = 123$ refers to collocation at triple points and relative to subregion Ω_1, and $\beta = 23$ refers to DOFs shared by $\partial\Omega_2$ and $\partial\Omega_3$. Finally, the right-hand sides f^γ, $\bar{f}^\gamma$ are obtained via (nodal or element) collocation of

$$\boldsymbol{c}(\boldsymbol{x}).\boldsymbol{u}^F(\boldsymbol{x}) + \int_{\Gamma_F(D)} \boldsymbol{T}^{(m)}(\boldsymbol{x},\boldsymbol{y},\omega).\boldsymbol{u}^F(\boldsymbol{y})dS_y, \tag{26}$$

Equations (23a,b,c,d) stem from nodal collocation on Γ_1, Γ_{12}, Γ_{12} and Γ_{123}, respectively, while equations (23e,f) stem from element collocation on Γ_{12} and Γ_{13}. Then, integral equation (22)

for the subdomain Ω_2 gives rise to the block matrix equations:

$$H_{12}^{21}\boldsymbol{u}^{12} + H_{123}^{21}\boldsymbol{u}^{123} + G_{12}^{21}\boldsymbol{t}^{12} + H_{23}^{21}\boldsymbol{u}^{23} - G_{23}^{21}\boldsymbol{t}^{23} = 0, \tag{27a}$$

$$H_{12}^{213}\boldsymbol{u}^{12} + H_{123}^{213}\boldsymbol{u}^{123} + G_{12}^{213}\boldsymbol{t}^{12} + H_{23}^{213}\boldsymbol{u}^{23} - G_{23}^{213}\boldsymbol{t}^{23} = 0, \tag{27b}$$

$$H_{12}^{23}\boldsymbol{u}^{12} + H_{123}^{23}\boldsymbol{u}^{123} + G_{12}^{23}\boldsymbol{t}^{12} + H_{23}^{23}\boldsymbol{u}^{23} - G_{23}^{23}\boldsymbol{t}^{23} = 0, \tag{27c}$$

$$\bar{H}_{12}^{21}\boldsymbol{u}^{12} + \bar{H}_{123}^{21}\boldsymbol{u}^{123} + \bar{G}_{12}^{21}\boldsymbol{t}^{12} + \bar{H}_{23}^{21}\boldsymbol{u}^{23} - \bar{G}_{23}^{21}\boldsymbol{t}^{23} = 0, \tag{27d}$$

$$\bar{H}_{12}^{23}\boldsymbol{u}^{12} + \bar{H}_{123}^{23}\boldsymbol{u}^{123} + \bar{G}_{12}^{23}\boldsymbol{t}^{12} + \bar{H}_{23}^{23}\boldsymbol{u}^{23} - \bar{G}_{23}^{23}\boldsymbol{t}^{23} = 0, \tag{27e}$$

with (27a,b,c) produced by nodal collocation on Γ_{21}, Γ_{213} and Γ_{23}, respectively, and (27d,e) by element collocation on Γ_{21} and Γ_{23}. In the subdomain Ω_3, sets of linear matrix equations may be defined as:

$$H_{13}^{31}\boldsymbol{u}^{13} + H_{123}^{31}\boldsymbol{u}^{123} + G_{13}^{31}\boldsymbol{t}^{13} + H_{23}^{31}\boldsymbol{u}^{23} + G_{23}^{31}\boldsymbol{t}^{23} + H_{3}^{31}\boldsymbol{u}^{3} = 0, \tag{28a}$$

$$H_{13}^{321}\boldsymbol{u}^{13} + H_{123}^{321}\boldsymbol{u}^{123} + G_{13}^{321}\boldsymbol{t}^{13} + H_{23}^{321}\boldsymbol{u}^{23} + G_{23}^{321}\boldsymbol{t}^{23} + H_{3}^{321}\boldsymbol{u}^{3} = 0, \tag{28b}$$

$$H_{13}^{32}\boldsymbol{u}^{13} + H_{123}^{32}\boldsymbol{u}^{123} + G_{13}^{32}\boldsymbol{t}^{13} + H_{23}^{32}\boldsymbol{u}^{23} + G_{23}^{32}\boldsymbol{t}^{23} + H_{3}^{32}\boldsymbol{u}^{3} = 0, \tag{28c}$$

$$H_{13}^{3}\boldsymbol{u}^{13} + H_{123}^{3}\boldsymbol{u}^{123} + G_{13}^{3}\boldsymbol{t}^{13} + H_{23}^{3}\boldsymbol{u}^{23} + G_{23}^{3}\boldsymbol{t}^{23} + H_{3}^{3}\boldsymbol{u}^{3} = 0, \tag{28d}$$

$$\bar{H}_{13}^{31}\boldsymbol{u}^{13} + \bar{H}_{123}^{31}\boldsymbol{u}^{123} + \bar{G}_{13}^{31}\boldsymbol{t}^{13} + \bar{H}_{23}^{31}\boldsymbol{u}^{23} + \bar{G}_{23}^{31}\boldsymbol{t}^{23} + \bar{H}_{3}^{31}\boldsymbol{u}^{3} = 0, \tag{28e}$$

$$\bar{H}_{13}^{32}\boldsymbol{u}^{13} + \bar{H}_{123}^{32}\boldsymbol{u}^{123} + \bar{G}_{13}^{32}\boldsymbol{t}^{13} + \bar{H}_{23}^{32}\boldsymbol{u}^{23} + \bar{G}_{23}^{32}\boldsymbol{t}^{23} + \bar{H}_{3}^{32}\boldsymbol{u}^{3} = 0, \tag{28f}$$

where equations (28a,b,c,d) stem from nodal collocation on Γ_{31}, Γ_{321}, Γ_{32} and Γ_3, respectively, while equations (28e,f) stem from element collocation on Γ_{31} and Γ_{32}. As previously pointed out, the set of equations (23a-f), (27a-e), (28a-f) is overdetermined. A square linear system of equations is obtained by setting up linear combinations of equations associated with the same collocation points and arising from different subdomains. For the present example, the square coupled BE-BE system consists of the following (combinations of) equations: (23a), (28d), α_u^{12}(23b)+α_u^{21}(27a), α_u^{13}(23c) +α_u^{31}(28a), α_u^{23}(27c)+α_u^{32}(28c), α_u^{123}(23d)+α_u^{213}(27b)+α_u^{321}(28b), α_t^{12}(23e)+α_t^{21}(27d), α_t^{13}(23f)+α_t^{31}(28e) and α_t^{23}(27e)+α_t^{32}(28f), where α_u^{ij} and α_t^{ij} are the weighting coefficients of the equations related to nodal collocations and element collocations respectively. This example thus involves weighted combinations of two equations and also, due to the presence of triple points, of three equations.

4.2 Implementation issues

This section aims at studying the choice of weighting coefficients, and other implementation issues such as scaling and unknowns ordering which also strongly affect the numerical efficiency and accuracy of the multi-domain FMM, with the help of a test problem having a known exact solution. All examples have been run on the same single-processor PC (RAM: 3GB, CPU frequency: 3.40 GHz).

4.2.1 Definition of the test problem

The test problem configuration is a spherical cavity subjected to an internal time-harmonic uniform pressure P, surrounded by two spherical shells embedded in an unbounded elastic medium (Fig. 8). The cavity surface and the two surrounding interfaces are concentric spheres with respective radii a_1, $a_2 = 2a_1$ and $a_3 = 3a_1$. Four sets (labelled a, b, c, d) of material properties, defined in Table 1, are used. Variations on this testing setup T will then be referred to using the following convention. Notation $T(a, b, c)$ refers to the "standard" two-shell, three-region configuration with materials a, b, c arranged in order of increasing radii.

Table 1. Definition of the mechanical properties for the test problem.

	ρ	μ	ν
a	3	4	0.25
b	6	5	0.25
c	2	1	1/3
d	2	1	0.25

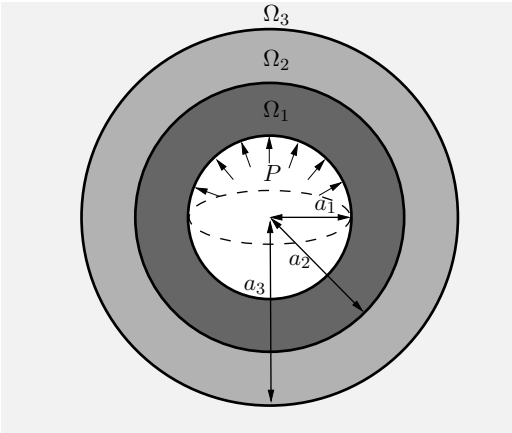

Figure 8. Definition of the test problem: spherical cavity under uniform pressure.

Testing configuration $T(a,b,b)$ then consists of three regions with the outermost two made of the same material, while $T(a,b)$ refers to just two regions defined by spheres of radii a_1, a_2 (i.e. $T(a,b,b)$ and $T(a,b)$ are physically identical but numerically treated as three-region and two-region configurations, respectively). This test problem has a closed-form analytical solution (see Appendix A).

4.2.2 Determination of optimal weightings

To determine suitable values for weighting coefficients α_u^{ij} and α_t^{ij}, some numerical experiments on two-region test configurations $T(d,d)$ (homogeneous) with $k_S^{(1)}a_1 = 7.64$ and $T(a,b)$ with $k_S^{(1)}a_1 = 4.68$ have been performed. In this case, the following set of equations are obtained using the linear combination procedure of Sec. 4.1:

$$\begin{aligned} H_1^1\boldsymbol{u}^1 + H_{12}^1\boldsymbol{u}^{12} - G_{12}^1\boldsymbol{t}^{12} - G_1^1\boldsymbol{t}_D^1 = 0, \\ \alpha_u^{12}\left[H_1^{12}\boldsymbol{u}^1 + H_{12}^{12}\boldsymbol{u}^{12} - G_{12}^{12}\boldsymbol{t}^{12} - G_1^{12}\boldsymbol{t}_D^1\right] + \alpha_u^{21}\left[H_{12}^{21}\boldsymbol{u}^{12} + G_{12}^{21}\boldsymbol{t}^{12}\right] = 0, \\ \alpha_t^{12}\left[\bar{H}_1^{12}\boldsymbol{u}^1 + \bar{H}_{12}^{12}\boldsymbol{u}^{12} - \bar{G}_{12}^{12}\boldsymbol{t}^{12} - \bar{G}_1^{12}\boldsymbol{t}_D^1\right] + \alpha_t^{21}\left[\bar{H}_{12}^{21}\boldsymbol{u}^{12} + \bar{G}_{12}^{21}\boldsymbol{t}^{12}\right] = 0, \end{aligned} \tag{29}$$

where $\boldsymbol{t}_D^1 = P\boldsymbol{e_r}$ is the traction applied on the inner sphere $r = a_1$. The mesh size is $N = 122,892$ ($\bar{\ell}_1 = 4$, $\bar{\ell}_2 = 4$, $d^{\min} = 0.30\lambda_S$). After having tried all 16 possible combinations where each weighting coefficient has value $\pm 1/2$, six of these combinations (defined in Table 2) were chosen to illustrate the effect of this choice on accuracy and convergence rate, the other ten being discarded as they all produced unsatisfactory results in terms of accuracy or convergence.

Table 3 shows the relative root mean square (RMS) errors $E(\boldsymbol{u}^1)$, $E(\boldsymbol{u}^{12})$ and $E(\boldsymbol{t}^{12})$

Table 2. Definition of the various set of coefficients used for determine the optimal one.

	1	2	3	4	5	6
α_u^{12}	0.5	0.5	0.5	−0.5	−0.5	−0.5
α_t^{12}	0.5	−0.5	−0.5	0.5	−0.5	−0.5
α_u^{21}	0.5	0.5	0.5	−0.5	0.5	−0.5
α_t^{21}	−0.5	0.5	−0.5	−0.5	0.5	0.5

Table 3. Solution error for the test problems $T(d,d)$ and $T(a,b)$, for the sets of coefficients listed in Table 2.

test problem	coefficient set	$E(\boldsymbol{u}^1)$	$E(\boldsymbol{u}^{12})$	$E(\boldsymbol{t}^{12})$	nb iter.
$T(d,d)$	1	/	/	/	> 300
	2	3.2×10^{-3}	2.5×10^{-3}	1.6×10^{-2}	64
	3	8.8×10^{-1}	8.8×10^{-1}	1.6×10^{0}	90
	4	/	/	/	> 300
	5	/	/	/	> 300
	6	/	/	/	> 300
$T(a,b)$	1	2.4×10^{-2}	1.7×10^{-2}	3.5×10^{-2}	94
	2	2.4×10^{-2}	1.8×10^{-2}	3.5×10^{-2}	22
	3	6.3×10^{-1}	4.7×10^{-1}	8.9×10^{-1}	2
	4	2.4×10^{-2}	1.7×10^{-2}	3.5×10^{-2}	122
	5	/	/	/	> 300
	6	2.4×10^{-2}	1.7×10^{-2}	3.5×10^{-2}	182

between the respective solutions $\boldsymbol{u}^1, \boldsymbol{u}^{12}, \boldsymbol{t}^{12}$ computed with the FMM and the corresponding analytical solution. On noting that $H_{12}^{12} = -H_{12}^{21}$, $G_{12}^{12} = G_{12}^{21}$, $\bar{H}_{12}^{12} = -\bar{H}_{12}^{21}$ and $\bar{G}_{12}^{12} = \bar{G}_{12}^{21}$ when subdomains 1 and 2 have the same material properties, sets 3 and 5 are seen to yield for $T(d,d)$ a singular and almost-singular matrix system, respectively. The poor results (in terms of either accuracy or convergence) achieved by sets 3 and 5 are not surprising in this light. Sets 1, 2, 4, 6 yield matrix systems that are made of rows of blocks that are identical except for their signs. The latter feature clearly has an effect on convergence properties, with set 2 exhibiting the best convergence rate. Hence, in the remainder of this article, integral equations collocated on all interfaces Γ_{ij} will be weighted according to $\alpha_u^{ij} = \alpha_u^{ji} = +0.5$ and $\alpha_t^{ij} = -\alpha_t^{ji} = -0.5$ $(i < j)$, as suggested by this test. Linear combinations of $p > 2$ block equations, which arise from collocation at nodes shared by p subregions (e.g. the triple points of the two-layered basin example of Sec. 4.1), are handled by assigning equal weight $1/p$ to each contributing block equation, an approach which has been successfully subjected to the test problem in its three-region form $T(a,b,c)$.

This approach, insofar as it exploits (combinations of) an initially overdetermined set of BEM matrix equations, may appear as computationally expensive. But, in fact, within a FMM framework, the additional number of collocation points only occurs on the interfacial surfaces Γ_{ij}. Moreover, only the CPU time of the last step of the FMM, namely the local expansion step which has been shown in Chaillat et al. (2008) to be of $O(N)$ complexity, is increased.

4.2.3 Equation scaling

Another simple but important detail of the present BE-BE coupling formulation is that convergence rates are improved by scaling equations. For multi-domain problems, the system

matrix is populated with various blocks whose magnitude depend on the material properties. Disparities in these magnitudes may lead to bad convergence rates. The introduction of scaling factors alleviates such problems. The following scaling factors are defined:

$$\tilde{g} = \frac{1}{n} \sum_{i=1}^{n} \frac{4\mu_i(1+\nu_i)}{(1-2\nu_i)} \tag{30}$$

$$\tilde{h} = \frac{1}{n} \sum_{i=2}^{n} d_i^{(0)} \tag{31}$$

where $(\mu_i,\ \nu_i)$ are the elastic properties of Ω_i and $d_i^{(0)}$ is the level-0 cell size in the octree introduced for Ω_i. We note that, due to the fact that Ω_1 is always the infinite medium, the domain size of Ω_1 is not taken into account in $\tilde{h}$. This scaling, a modified version of that used in Araújo et al. (2001) which includes the effect of the domain size, is equivalent to introducing new, non-dimensional, unknowns $\tilde{\boldsymbol{u}}^{ij}$ and $\tilde{\boldsymbol{t}}^{ij}$:

$$\begin{aligned} \boldsymbol{u}^{ij} &= \tilde{h}\ \tilde{\boldsymbol{u}}^{ij} \\ \boldsymbol{t}^{ij} &= \tilde{g}\ \tilde{\boldsymbol{t}}^{ij} \end{aligned} \tag{32}$$

and replacing the block matrices H and G with $\tilde{H} = \tilde{h}\ H$ and $\tilde{G} = \tilde{g}\ G$. Using this scaling, all coefficients of the resulting coupled system have similar magnitudes. Some results on the efficiency of the introduction of this scaling are presented in Section 5.1 on seismological problems involving an infinite medium Ω_1.

4.2.4 Other implementation issues

In keeping with the modular approach previously outlined, where FMM is applied separately for each subregion, separate BE meshes are defined for each subdomain, with meshes for two adjacent subdomains being compatible over the shared interface. Each adjacent mesh is oriented relative to its subdomain. This method ensures that normals to all elements of a given subdomain have a consistent (outward) orientation.

Another important issue is the iterative solver convergence rate. For multi-domain problems, both displacements and tractions are unknown at the interfaces. Optimal ordering of the matrix blocks for a multi-zone boundary element analysis is very important when using an iterative solver (GMRES for example). Here, one may order the unknown DOF subvectors (i.e. block columns) arbitrarily, but should then use the same order for the sets of collocation points (i.e. block rows), so as to define the global matrix closest to a symmetric matrix. For example, for the test problem $T(a,b)$ ($N = 122,892$; $k_S^{(1)} a_1 = 4.68$), a suitably ordered governing matrix is

$$\begin{bmatrix} H_1^1 & H_{12}^1 & -G_{12}^1 \\ 0.5H_1^{12} & 0.5H_{12}^{12} + 0.5H_{12}^{21} & -0.5G_{12}^{12} + 0.5G_{12}^{21} \\ -0.5\bar{H}_1^{12} & -0.5\bar{H}_{12}^{12} + 0.5\bar{H}_{12}^{21} & 0.5\bar{G}_{12}^{12} + 0.5\bar{G}_{12}^{21} \end{bmatrix} \tag{33}$$

so that collocation points (lines) and unknowns (columns) are ordered similarly (displacements on external surfaces, then displacements on interfaces, then tractions on interfaces). With this ordering, GMRES converges (with relative tolerance 10^{-3}) after only 22 iterations. Swapping the second and first lines in (33) results in a failure of GMRES to converge within $1,000$ iterations, whereas swapping also the second and third columns in (33) restores satisfactory convergence within 22 iterations.

Table 4. Homogeneous test problems: relative RMS error.

Test pb.	N	$\frac{d^{\min}}{\lambda_S^{(1)}}$	$k_S^{(1)}a_1$	$\bar{\ell}_i$	$E(\boldsymbol{u}^1)$	$E(\boldsymbol{u}^{12})$	$E(\boldsymbol{t}^{12})$	$E(\boldsymbol{u}^{23})$	$E(\boldsymbol{t}^{23})$	nb iter.
$T(d,d)$	$30,732$	0.30	3.54	$3;3$	1.3×10^{-2}	4.7×10^{-3}	1.7×10^{-2}	/	/	6
$T(d,d)$	$122,892$	0.30	7.64	$4;4$	3.0×10^{-3}	2.5×10^{-3}	1.6×10^{-2}	/	/	64
$T(d,d,d)$	$57,778$	0.21	3.54	$3;3;3$	8.3×10^{-3}	9.4×10^{-3}	4.5×10^{-2}	1.2×10^{-2}	3.4×10^{-2}	31
$T(d,d,d)$	$215,058$	0.30	7.64	$3;4;4$	6.1×10^{-3}	7.7×10^{-3}	2.2×10^{-2}	6.6×10^{-3}	2.0×10^{-2}	864

Table 5. Heterogeneous test problems: relative RMS error.

Test pb.	N	$\frac{d^{\min}}{\lambda_S^{(1)}}$	$k_S^{(1)}a_1$	$\bar{\ell}_i$	$E(\boldsymbol{u}^1)$	$E(\boldsymbol{u}^{12})$	$E(\boldsymbol{t}^{12})$	$E(\boldsymbol{u}^{23})$	$E(\boldsymbol{t}^{23})$	nb iter.
$T(a,b)$	$30,732$	0.17	2.17	$3;3$	5.0×10^{-3}	5.1×10^{-3}	1.6×10^{-2}	/	/	21
$T(a,b)$	$122,892$	0.30	4.93	$3;4$	2.4×10^{-2}	1.8×10^{-2}	3.5×10^{-2}	/	/	22
$T(a,b,c)$	$57,778$	0.13	2.17	$3;3;3$	3.0×10^{-2}	1.4×10^{-2}	2.2×10^{-2}	1.3×10^{-2}	2.8×10^{-2}	59
$T(a,b,c)$	$215,058$	0.30	4.93	$3;3;4$	1.0×10^{-2}	1.3×10^{-2}	1.0×10^{-2}	1.4×10^{-2}	1.4×10^{-2}	43

4.3 Accuracy and computational efficiency of multi-domain FM-BEM

Our implementation of elastodynamic FMM was validated for single-region problems in Chaillat et al. (2008), in terms of accuracy and computational efficiency on the simple test case of a pressurized spherical cavity, with observed computing times consistent with the theoretical complexity $O(N \log N)$ and accuracy similar to that of the standard (i.e. non-FMM) BEM.

To validate the present BE-BE coupling, the test problem of Section 4.2.1 is again considered. The frequency is adjusted so that the mesh features at least 10 points per S-wavelength in all cases.

Considering first homogeneous cases $T(d,d)$ and $T(d,d,d)$, Table 4 shows the number of degrees of freedom, the leaf-cell size parameter $d^{\min}$, the normalized frequency of the problem, the leaf level $\bar{\ell}$ and the relative root mean square (RMS) error $E(\boldsymbol{u}^1)$, $E(\boldsymbol{u}^{12})$, $E(\boldsymbol{t}^{12})$, $E(\boldsymbol{u}^{23})$ and $E(\boldsymbol{t}^{23})$. In this example, we observe that the precision of the FM-accelerated BEM is acceptable for $d^{\min} \geq 0.30\lambda_S$, consistently with earlier findings in Chaillat et al. (2008). The bad conditioning of the matrix, and the fact that the number of iterations rapidly increases with the problem size, are also manifest, which emphasizes the desirability of a good preconditioning strategy (not yet implemented). The same data is next given in Table 5 for heterogeneous test problems $T(a,b)$ and $T(a,b,c)$, which exhibit much better convergence properties.

5 PROPAGATION AND AMPLIFICATION OF SEISMIC WAVES IN ALLUVIAL BASINS

In Chaillat et al. (2008), the single-domain elastodynamic FMM has been compared to the results of Sánchez-Sesma (1983) for the scattering by an irregular homogeneous half-space of a plane vertical P-wave at normalized frequency $k_P a/\pi = 0.25$ (with $\nu = 0.25$), and then applied to the same configuration at a higher frequency ($k_P a/\pi = 5$). In this section, the

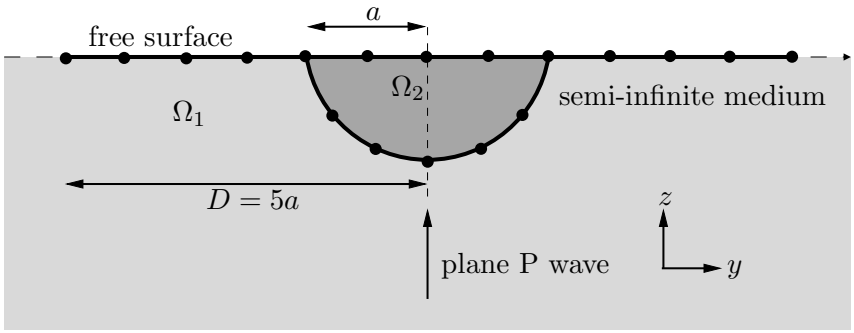

Figure 9. Propagation of an incident plane P-wave in a semi-spherical alluvial basin: notations.

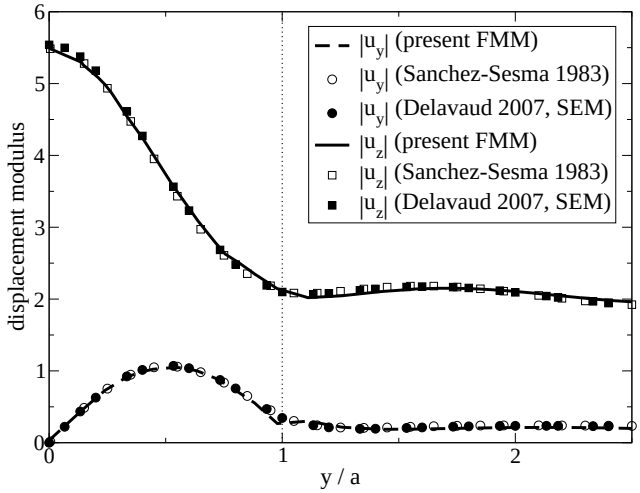

Figure 10. Propagation of an incident plane P-wave in a semi-spherical alluvial basin: surface displacement at $k_P^{(1)}a/\pi = 0.5$ and comparisons with Sánchez-Sesma (1983) and Delavaud (2007).

present multi-domain implementation is applied to the propagation of seismic waves in alluvial basins. Unless indicated otherwise, all examples have been run on the same single-processor PC (RAM: 3GB, CPU frequency: 3.40 GHz).

5.1 Seismic wave propagation in canonical basins

5.1.1 Validation on a simple example

This first example is concerned with the propagation in a semi-spherical alluvial basin (i.e. soft elastic inclusion) of a plane P-wave of unit amplitude traveling vertically in an elastic homogeneous irregular half-space (Fig. 9). Such a configuration may lead to a strong amplification of the seismic motion in soft alluvial deposits.

As in Sánchez-Sesma (1983), we investigate the motion at the surface of the alluvial basin Ω_2, for the following values of the material parameters: $\mu^{(2)} = 0.3\mu^{(1)}$, $\rho^{(2)} = 0.6\rho^{(1)}$, $\nu^{(1)} = 0.25$ and $\nu^{(2)} = 0.3$. The normalized frequency is defined by $k_P^{(1)}a/\pi$ in terms of the properties of the elastic semi-infinite medium Ω_1. The radius of the discretized free surface is set to $D = 5a$.

The surface displacements computed with the present multi-domain FMM are presented, along with corresponding results from Sánchez-Sesma (1983) (using series expansion method)

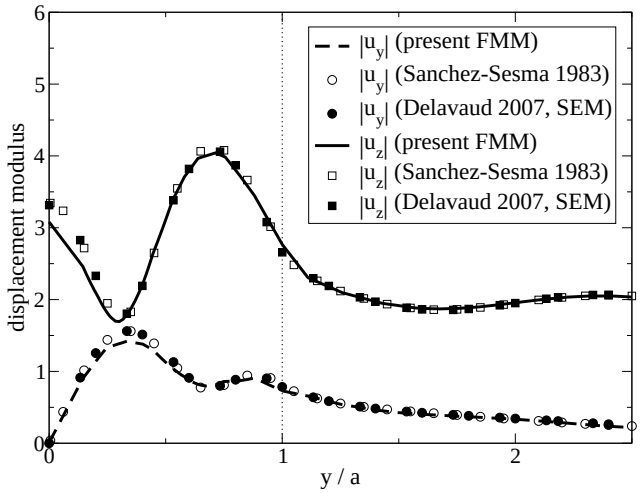

Figure 11. Propagation of an incident plane P-wave in a semi-spherical alluvial basin: surface displacement at $k_P^{(1)} a/\pi = 0.7$ and comparisons with Sánchez-Sesma (1983) and Delavaud (2007).

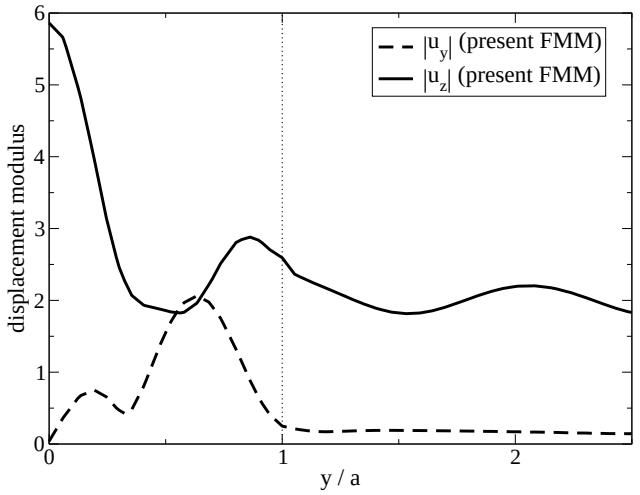

Figure 12. Propagation of an incident plane P-wave in a semi-spherical alluvial basin: surface displacement at $k_P^{(1)} a/\pi = 1$.

Table 6. Propagation of an incident plane P-wave in a semi-spherical alluvial basin: data and computational results.

$k_P^{(1)} a/\pi$	N	$d^{\min}/\lambda_S$	$\bar{l}_1; \bar{l}_2$	CPU (s) / iter	nb iter. (a)	nb iter. (b)	nb iter. (c)
0.5	17,502	0.15	3; 3	8	28	44	86
0.7	17,502	0.21	4; 3	10	34	60	111
1	90,057	0.30	4; 3	49	52	192	519
2	190,299	0.30	5; 4	79	325	3,006	$> 5,000$

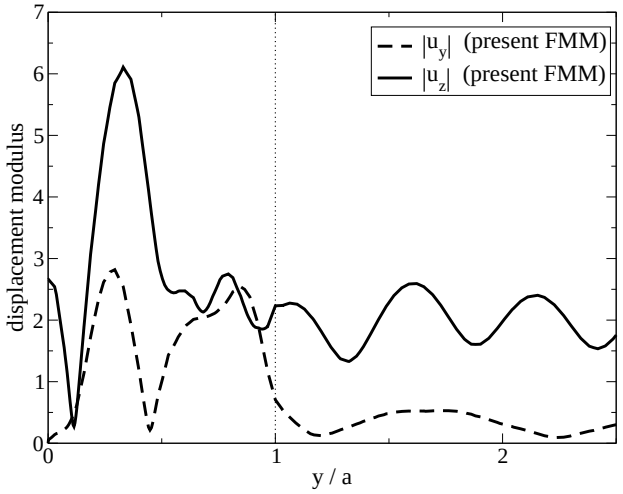

Figure 13. Propagation of an incident plane P-wave in a semi-spherical alluvial basin: surface displacement at $k_P^{(1)}a/\pi = 2$.

and Delavaud (2007) (using spectral element method), for $k_P^{(1)}a/\pi = 0.5$ (Fig. 10) and $k_P^{(1)}a/\pi = 0.7$ (Fig. 11). All results are seen to be in good agreement. For those examples, a leaf-cell size $d^{\min}$ lower than the threshold $d^{\min} = 0.30\lambda_S$ recommended in Chaillat et al. (2008) had to be used as a consequence of the chosen truncation radius $D = 5a$, allowing to compare our results to the previously-published ones. Additionally, the FMM allowed to perform computations at higher frequencies $k_P^{(1)}a/\pi = 1$ (Fig. 12) and $k_P^{(1)}a/\pi = 2$ (Fig. 13), for which no published results are available for comparison purposes. For such higher frequencies, the maximum amplification level is seen to range from 2 to 3 (free surface effects being removed). In Table 6, the number of DOFs, the size of the leaf cells and the leaf level $\bar{\ell}_i$ in each subdomain Ω_i are given for the meshes used, together with the CPU time per iteration recorded. Those examples are also used to illustrate the efficiency of the scaling factors introduced in Section 4.2.3. Iteration counts using three different scalings are given in Table 6: (a) using the scaling factor introduced in Section 4.2.3; (b) using a modified version of (a):

$$\tilde{h} = \frac{1}{n}\sum_{i=1}^{n} d_i^{(0)}$$

and (c) without any scaling. Scaling (a) is seen to perform best. It can be easily understood that scaling (b) is less efficient since it incorporates a characteristic size for the (truncated) infinite medium Ω_1. The equation scaling (a) is very efficient and drastically reduces (by up to 90%) the iteration counts. However, the last example also indicates that the iteration count significantly impacts the computational efficiency for problem sizes for which the CPU time per iteration and the memory requirements are still moderate. An efficient preconditioning strategy is clearly needed, and will be addressed in future investigations.

5.1.2 Influence of the truncation radius D

In Sánchez-Sesma (1983), the size of the discretized free surface is set to $D = 5a$. A natural issue concerns the selection of the best value of the truncation radius D for the model, i.e. the smallest value of D for which the solution is practically insensitive to the free-surface truncation. Taking advantage of the larger problem sizes allowed by the present FMM, this

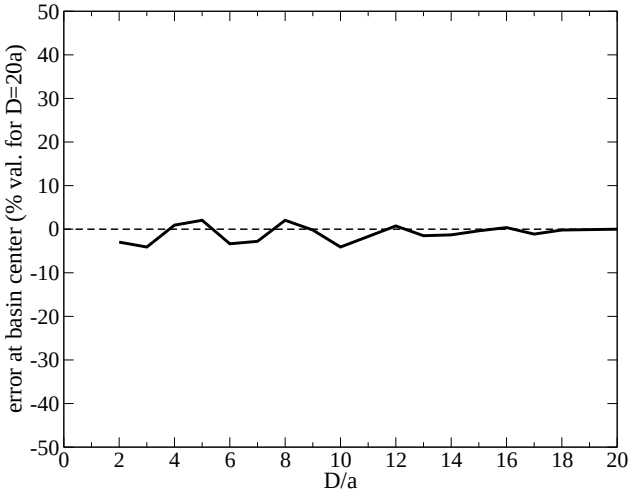

Figure 14. Propagation of an incident plane P-wave in a semi-spherical basin: discrepancy between the reference solution ($D = 20a$) and solutions obtained for various truncation radii D at the basin center.

Table 7. Propagation of an incident plane P-wave in a semi-spherical basin: discrepancy between the reference solution ($D = 20a$) and solutions obtained for various truncation radii D, at three surface points (in % of the reference solution).

D/a	2	4	6	8	10	12	14	16	18
$r = 0$	−2.97	0.93	−3.35	2.05	−4.09	0.74	−1.30	0.37	−0.19
$r = a/2$	−1.85	−0.31	−2.33	−0.02	−2.46	0.38	−1.30	−0.20	−0.35
$r = 3a/2$	0.68	0.19	0.23	−0.22	0.59	−0.27	0.24	−0.01	0.41

issue is now investigated by means of a parametric study. The choice of D obviously depends on the size of the region for which a truncation-insensitive numerical solution is sought. Here, the latter is chosen such that $r/a \leq 3$. A similar study, restricted to $D \leq 5a$, has been done in Niu & Dravinski (2003) in the case of the diffraction of a plane P wave by a semi-spherical canyon.

Figure 14 shows the relative difference between the solution computed at the center of the basin for several truncation radii D and a reference solution obtained for $D = 20a$, at normalized frequency $k_P^{(1)} a/\pi = 0.5$. These results suggest that the convergence is achieved for $D \geq 13a$ ($= 13\lambda_P^{(1)}/4 > 3\lambda_P^{(1)}$) and that, for $D < 13a$, the error with respect to the reference solution oscillates within a range $\pm 4\%$. Here, it can be seen that the value $D = 5a$ used in Sánchez-Sesma (1983) yields reasonably, but not optimally, accurate results at the basin center. This parametric study is conducted for the displacement at the center of the basin because errors caused by truncation are observed to be largest there. In fact, for $r/a \geq 0.5$, the sensitivity of the results to the choice of D was found to be low (see Table 7).

5.2 Propagation of an incident plane P-wave in a two-layered semi-spherical basin

The results of section 5.1 are limited to a single-layered basin, whereas the present implementation is applicable to more general configurations featuring piecewise-homogeneous basins. To demonstrate this capability, the propagation of an incident plane P-wave in a heteroge-

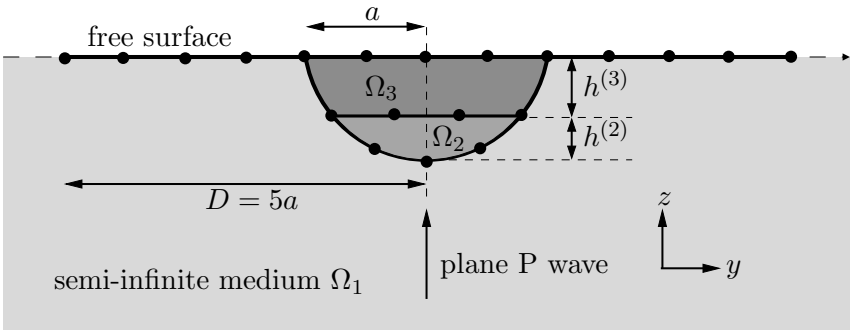

Figure 15. Propagation of an incident plane P-wave in a two-layered semi-spherical basin: notation.

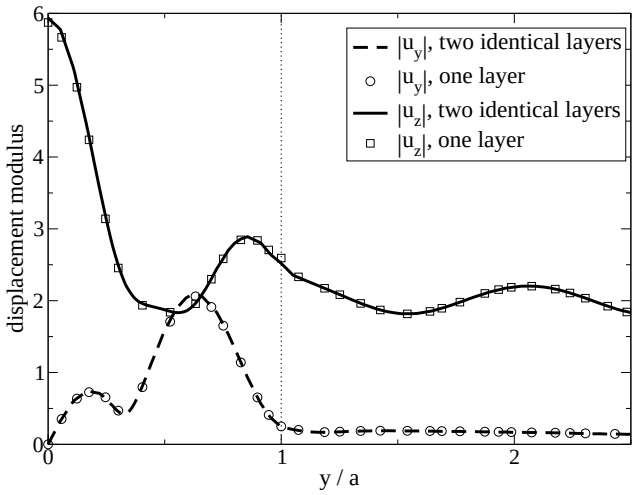

Figure 16. Propagation of an incident plane P-wave in a two-layered semi-spherical basin (with the same material in Ω_2 and Ω_3 and $k_P^{(1)}a/\pi = 1$): comparison with the result for a one-layered semi-spherical basin (Fig. 12).

neous semi-spherical basin is now considered for an alluvial deposit composed of two layers (Fig. 15).

5.2.1 Validation: two layers involving identical materials

First, to check our implementation in the multi-domain case, identical mechanical properties are assumed for Ω_2 and Ω_3:

$$\mu^{(2)} = \mu^{(3)} = 0.3\mu^{(1)},\ \rho^{(2)} = \rho^{(3)} = 0.6\rho^{(1)},\ \nu^{(1)} = 0.25,\ \nu^{(2)} = \nu^{(3)} = 0.3.$$

The study is performed at normalized frequency $k_P^{(1)}a/\pi = 1$, using a truncation radius $D = 5a$. The mesh features $N = 91,893$ DOFs. The results of this computation, which took 81 iterations and 48s per iteration ($\bar{\ell}_1 = 4$; $\bar{\ell}_2 = 3$; $\bar{\ell}_3 = 3$), are seen in Figure 16 to coincide (as they should) with those computed with a single-layered basin (Fig. 12).

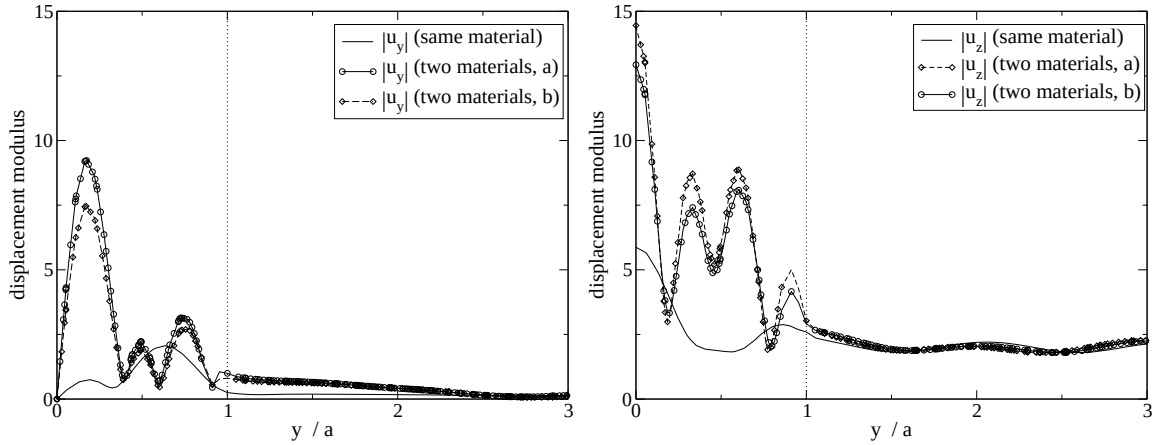

Figure 17. Propagation of an incident plane P-wave in a two-layered semi-spherical basin (with mechanical properties (34) and (35) , $k_P^{(1)}a/\pi = 1$).

5.2.2 Two-layered heterogeneous basin

Now, the two layers Ω_2 and Ω_3 are made of different materials. Symbols $\chi_P^{(ij)}$ and $\chi_S^{(ij)}$ will be used to denote the P-wave and S-wave velocity contrasts:

$$\chi_P^{(ij)} = c_P^{(j)}/c_P^{(i)}; \qquad \chi_S^{(ij)} = c_S^{(j)}/c_S^{(i)}$$

Two examples are considered. In example (a), mechanical properties are defined so that $\chi_S^{(12)}$ is the same as in section 5.1 and as in Sánchez-Sesma (1983), and that $\chi_S^{(12)} = \chi_S^{(23)}$:

$$\frac{\rho^{(2)}}{\rho^{(1)}} = \frac{\rho^{(3)}}{\rho^{(2)}} = 0.6; \quad \frac{\mu^{(2)}}{\mu^{(1)}} = \frac{\mu^{(3)}}{\mu^{(2)}} = 0.3; \quad \nu^{(1)} = 0.25; \quad \nu^{(2)} = \nu^{(3)} = 0.30 \tag{34}$$

In example (b), the velocity contrasts between Ω_1, Ω_2 and Ω_2, Ω_3 are the same for P- and S-waves, $\chi_S^{(12)} = \chi_S^{(23)}$ and $\chi_P^{(12)} = \chi_P^{(23)}$:

$$\frac{\rho^{(2)}}{\rho^{(1)}} = \frac{\rho^{(3)}}{\rho^{(2)}} = 0.6; \quad \frac{\mu^{(2)}}{\mu^{(1)}} = \frac{\mu^{(3)}}{\mu^{(2)}} = 0.3; \quad \nu^{(1)} = 0.25; \quad \nu^{(2)} = 0.30; \quad \nu^{(3)} = 0.34 \tag{35}$$

The thickness, $h^{(2)}$ and $h^{(3)}$ of the layers Ω_2 and Ω_3 are adjusted to the wavelengths:

$$h^{(2)}/\lambda_S^{(2)} = h^{(3)}/\lambda_S^{(3)} \quad \Rightarrow \quad h^{(2)} = \sqrt{2}h^{(3)} = (2-\sqrt{2})a \tag{36}$$

The mesh and normalized frequency ($k_P^{(1)}a/\pi = 1$) are the same as in the homogeneous case of Sec. 5.2.1. The computations required 255 and 272 iterations for example (a) and (b), respectively, and 48s per iteration ($\bar{\ell}_1 = 4$; $\bar{\ell}_2 = 3$; $\bar{\ell}_3 = 3$).

On Figure 17, the results of the computations (a) and (b) for the two-layered semi-spherical basin are compared to those for a single-layered basin (Fig. 12). The introduction of the layer Ω_3 leads to stronger amplification (up to 7 for (a) or 6.5 for (b) instead of 3 for the single-layered basin, the free-surface effects being removed), with shorter wavelengths in the basin. We also see on this example the effect of the value of $\nu^{(3)}$: a higher value of $\nu^{(3)}$ leads to a smaller increase of the maximum amplification.

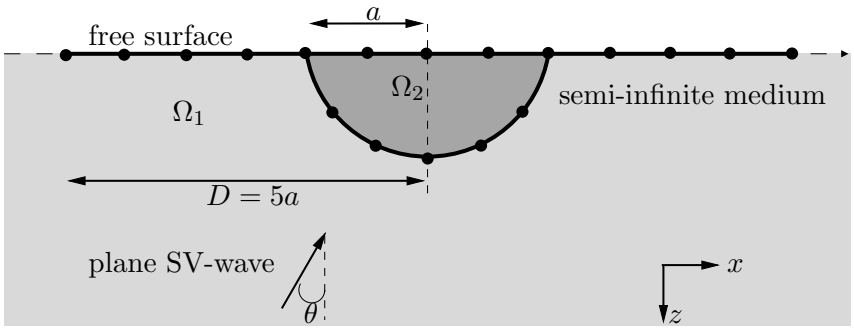

Figure 18. Propagation of an oblique incident plane SV-wave in a semi-spherical basin: notation.

5.3 SV-wave amplification in a semi-spherical basin

All examples presented so far in this section involve incident P-waves. However, a fully 3D validation requires considering other types of incident fields such as plane SV-waves with oblique incidence. Such configurations have been studied by Mossessian & Dravinski (1990a,b) using standard indirect BEM. In this section, the propagation of a plane SV-wave in a semi-spherical basin is considered in both the frequency domain and the time domain. As the Fourier synthesis of the time domain solution requires many FMM analyses at various frequencies, the results presented in this section have been obtained on a 8-processor PC (RAM: 32GB, CPU frequency: 2.33 GHz), each FMM analysis being performed independently on a single processor.

5.3.1 Problem definition

This example is concerned with the propagation in a semi-spherical basin of an oblique incident plane SV-wave of unit amplitude traveling in an elastic half space (see Fig. 18). A right-handed Cartesian frame (x, y, z) is defined so that the elastic half-space occupies the region $\{(x, y, z) \,|\, z \geq 0\}$. The truncation radius is $D = 5a$. This configuration has been studied in the time domain in Mossessian & Dravinski (1990a) and in the frequency domain in Mossessian & Dravinski (1990b) using a standard indirect BEM (with the half-space Green's functions). The mechanical parameters are defined as follows: $c_S^{(1)} = 1\text{m.s}^{-1}$, $c_P^{(1)} = 2\text{m.s}^{-1}$, $\mu^{(2)}/\mu^{(1)} = 1/6$, $\rho^{(2)}/\rho^{(1)} = 2/3$ and $\nu^{(1)} = \nu^{(2)} = 1/3$. In Mossessian & Dravinski (1990a,b), a weakly inelastic formulation (with P-wave and S-wave quality factors equal to 100) is used whereas our FMM implementation is purely elastic.

5.3.2 Synthesis of the time domain solution

The time domain response $\boldsymbol{u}(\boldsymbol{x}, t)$ can be computed using an inverse Fourier transform:

$$\boldsymbol{u}(\boldsymbol{x}, t) = \mathcal{F}^{-1}\Big(\tilde{\boldsymbol{u}}(\boldsymbol{x}, \omega)\boldsymbol{s}(\omega)\Big), \tag{37}$$

where $\tilde{\boldsymbol{u}}(\boldsymbol{x}, \omega)$ is the frequency domain solution and $s(\omega)$ is the source spectrum. In practice, a Fast Fourier Transform is used to synthetize the time domain results. In the following, the source spectrum is a second-order Ricker wavelet:

$$\begin{aligned} \boldsymbol{s}(t) &= \Big(2\pi^2\frac{(t-t_s)^2}{t_p^2} - 1\Big)\exp\Big[-\pi^2\frac{(t-t_s)^2}{t_p^2}\Big] \\ \Rightarrow \quad \boldsymbol{s}(\omega) &= -\frac{\sqrt{\pi}\omega^2 t_p^3}{2\pi^3}\exp\Big[-\frac{\omega^2}{4\pi^2}t_p^2\Big]\exp\Big[-i\omega t_s\Big] \end{aligned} \tag{38}$$

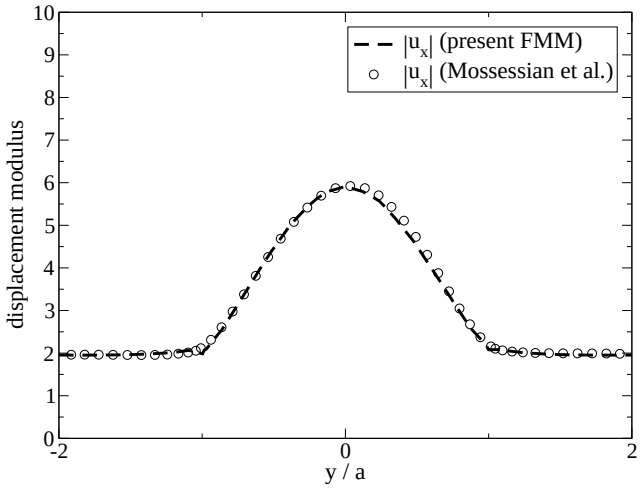

Figure 19. Propagation of a vertical ($\theta = 0°$) incident plane SV-wave in a semi-spherical basin: Comparison of the FMM computed displacements (x-component) with the results of Mossessian & Dravinski (1990b).

where t_s is the time related to the maximum amplitude of the wavelet and t_p is the fundamental period of the signal. The fundamental frequency of such a wavelet is $f_0 = 1/t_p$.

An important numerical issue in the present approach lies with the meshes used. Usually, the mesh size is adjusted so that, for the frequency $f = 2f_0$, the mesh contains about ten points per S-wavelength. However, when using the FMM, this approach is not the most efficient as if the same mesh is used for all computations, the mesh density for low frequency computations is high relative to wavelength, increasing the computational burden for the near contributions, multipole moments and local expansions. Moreover, memory requirements are also increased. On the other hand, to perform the synthesis, the solutions for each frequency need to be eventually defined on the same mesh. A simple improvement, used here, exploits a hierarchical sequence of meshes $\mathcal{M}_0, \mathcal{M}_1, \ldots$ where the coarser mesh $\mathcal{M}_0$ is adjusted (using the 10-points-per-S-wavelength criterion) to the lowest frequency and $\mathcal{M}_{k+1}$ is obtained by splitting each triangle of $\mathcal{M}_k$ into four subtriangles. Then, the solutions obtained on coarser meshes $\mathcal{M}_0, \ldots, \mathcal{M}_{n-1}$ are linearly interpolated on the finest mesh $\mathcal{M}_n$.

5.3.3 Validation in frequency domain

The example depicted in Fig. 18 has been treated, for a normalized frequency $k_S^{(1)} a/\pi = 0.5$ and for $\theta = 0°, 30°$. The mesh features $N = 17,502$ DOFs. The computations take 5s per iteration, 32 iterations for the case $\theta = 0°$ and 34 iterations for the case $\theta = 30°$ ($\bar{\ell}_1 = 3$, $\bar{\ell}_2 = 3$, $d_{\min} = 0.25\lambda_S$).

For the case $\theta = 0°$ (resp. $\theta = 30°$), the x-components (resp. x-, y- and z-components) of the computed displacements on the surface are displayed in Fig. 19 (resp. Fig. 20). They are in good agreement with the results of Mossessian & Dravinski (1990b) even though, in our implementation, no attenuation is considered.

5.3.4 Time-domain response

Once the implementation validated in the frequency domain, the time domain response is considered for $\theta = 30°$. To allow comparisons, the fundamental frequency of the source is set

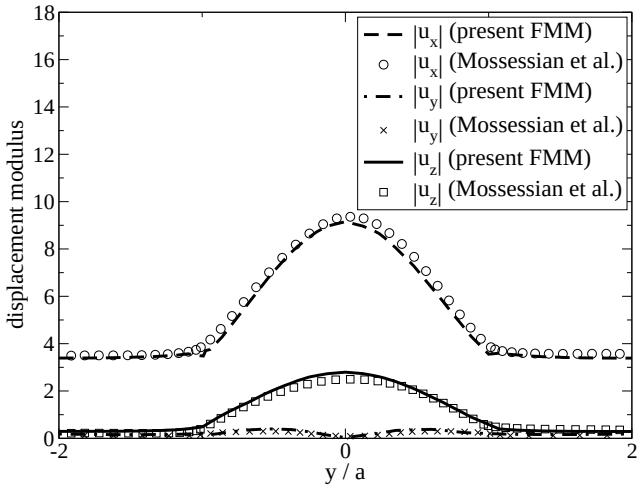

Figure 20. Propagation of an oblique ($\theta = 30°$) incident plane SV-wave in a semi-spherical basin: Comparison of the FMM computed displacements (x-, y- and z-components) with the results of Mossessian & Dravinski (1990b).

to a relatively low value: $f_0 = 0.25$ Hz ($t_p = 4s$ and $t_s = 5s$). In this example, only one mesh is used, featuring $N = 36,033$ DOFs.

Frequency parametrization. Results are computed for frequencies ranging between 0 and 0.85 Hz (32 sample frequencies). Figure 21 displays the x- and z-components of spectral displacement along the Ox and Oy axes for the sample frequencies. The fundamental frequency is found about 0.30 Hz ($k_p^{(2)} a/\pi = 0.60$) in all four shown cases. The maximum amplification against the Ox axis and for the x-component is seen to be about 13.15 (free-surface effect being removed) and located at a higher frequency (f=0.735Hz) at the left of the basin center ($x/a = -0.4$) while for the z-component, this maximum is also located at the left of the basin center ($x/a = -0.2$) but with about half amplification (about 6.15). A unique maximum is obtained for the x-component while for the z-component, several local maxima of amplification are obtained. The maximum amplification (about 13.3) for the x-component of the displacement against the Oy axis is obtained at the basin center for a high frequency (f=0.74Hz) while for the z-component this maximum (about 5.2) is obtained for a frequency of about 0.685Hz. Once again, the maximum amplification for the x-component is about twice the maximum amplification for the z-component. If we consider a 1D layer (having the same properties) on a half-space, the fundamental frequency is reduced to $f_0 = c_S^{(2)}/4a = 0.125$Hz ($k_p^{(2)} a/\pi = 0.25$) and the maximum amplification is also reduced to $\rho^{(1)} c_S^{(1)} \ / \ \rho^{(2)} c_S^{(2)} = 3$. This simple example illustrates the usefulness of 3D models to study seismic wave amplification in alluvial basins.

Displacements against time. The time domain results obtained from spectral responses are now presented. The x- and z- components of the displacement for $t \in [0, 30]$ are plotted against the Ox and Oy axes in Figs. 22 and 23, respectively.

These results, visually compared with those previously published by Mossessian & Dravinski (1990b), validate our implementation. We note on these figures that the time domain amplification is lower than the spectral amplification. It is due to the fact that in time domain, the propagation process also influences the signal duration. To investigate this parameter, we use the definition proposed in Trifunac & Brady (1975). In Fig. 24, the integrals $\int u_x^2 dt$ and $\int u_z^2 dt$ are displayed against time. The duration of displacement at the basin center is estimated on that basis as about 5.9s (for the x-component) and 8.4s (for the z-component) while the duration of the input signal is estimated as about 3.7s.

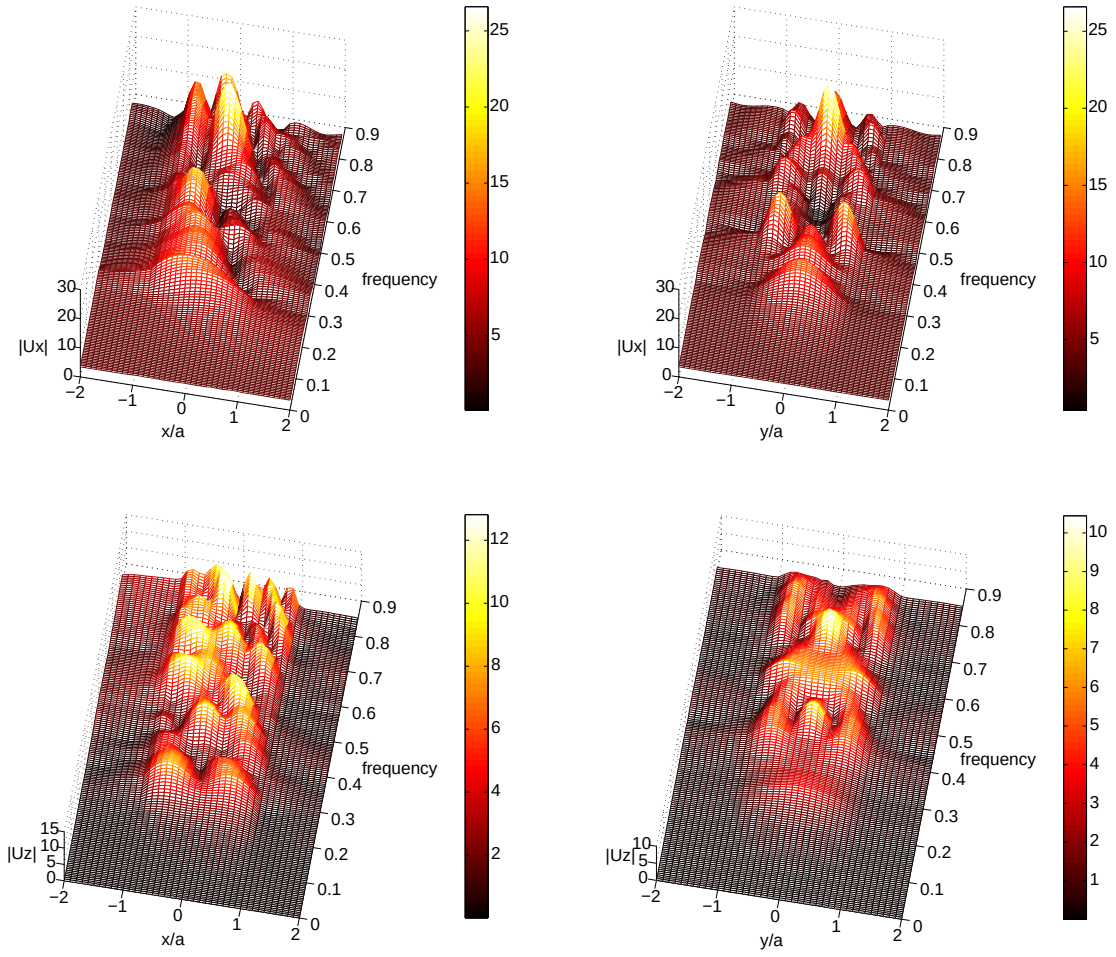

Figure 21. Propagation of an oblique ($\theta = 30°$) incident plane SV-wave in a semi-spherical alluvial basin: x- (top) and z-component (bottom) of the FMM computed displacement against the x (left) and y (right) coordinate for the sample frequencies.

5.3.5 Higher fundamental frequency

The use of the FM-BEM allows us to consider higher fundamental frequency, for which no published results are available for comparison purposes. The following results are concerned with the same problem of an oblique incident plane SV-wave propagating in a semi-spherical basin but for a fundamental frequency twice higher: $f_0 = 0.50$Hz ($t_p = 2$s and $t_s = 5$s). In this example, two meshes are used: $\mathcal{M}_0$, featuring $N = 36,033$ DOFs and $\mathcal{M}_1$ (created using the subdivision procedure explained in Section 5.3.2), featuring $N = 143,451$ DOFs. For this computation, 64 sample frequencies have been used, for frequencies ranging between 0 and 1.70Hz. The x- and z- components of the displacement for $t \in [0, 30]$ are plotted against the Ox and oy axes in Figs. 25 and 26, respectively.

We note on those figures that doubling the fundamental frequency led to an increase of the maximum amplification for all the components (see scales in Figs 25 and 26). Once again, the duration of the displacement is estimated. In Figure 27, the integrals $\int u_x^2 dt$ and $\int u_z^2 dt$ are respectively displayed against time, leading to estimated values of about 11.5s (x-component) and 10s (z-component) for the duration of displacement. Doubling the fundamental frequency

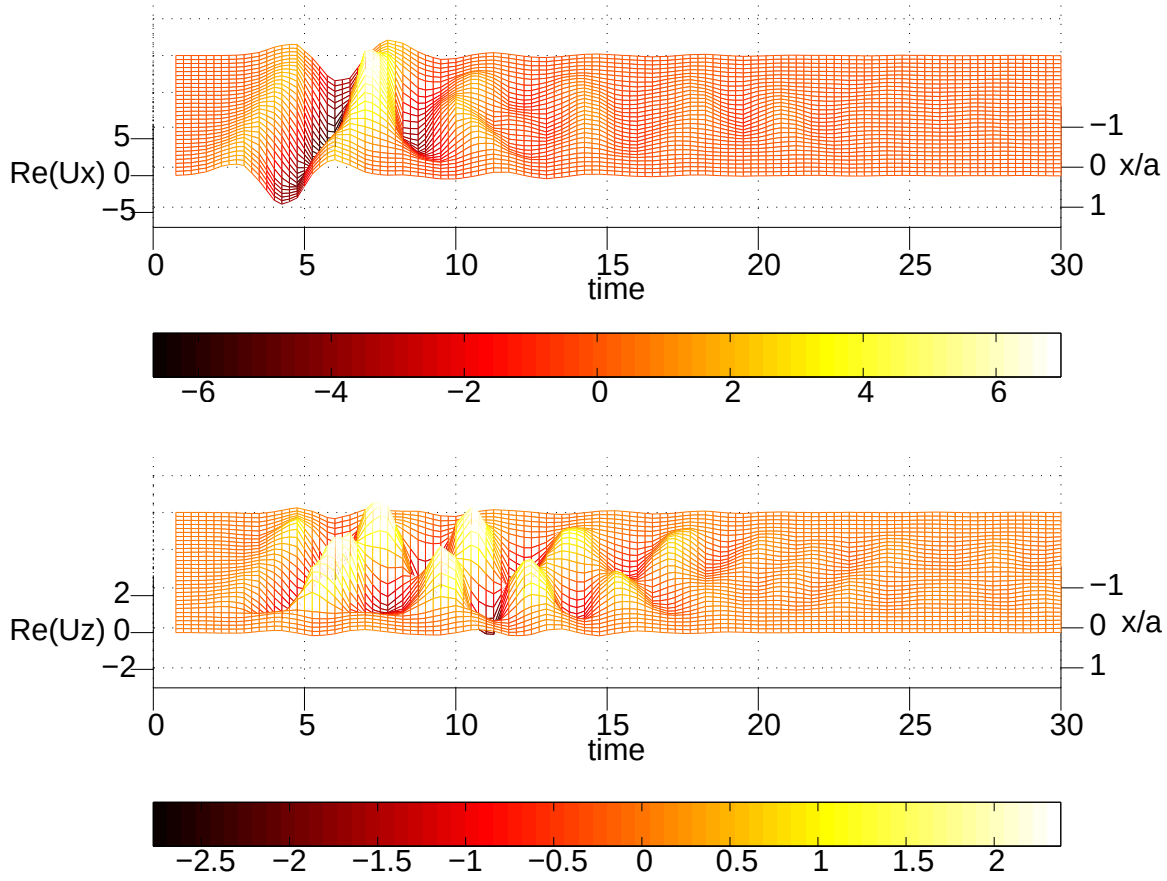

Figure 22. Propagation of an oblique ($\theta = 30°$) incident plane SV-wave in a semi-spherical alluvial basin, $f_0 = 0.25$Hz: x- (top) and z-components (bottom) of FMM computed displacement along the Ox axis against time.

thus induces a double duration of the x-component but only a small increase of the duration of the z-component.

5.3.6 Conclusions on the use of the present FMM for time domain problems

Using standard BEM, the resolution of time domain responses was limited in terms of sampling frequency range. Introducing the FMM enlarges the capabilities of the BEM in this respect, and time domain responses with higher fundamental frequencies are now possible. In section 5.3.5, a computation for a fundamental frequency twice higher that in Mossessian & Dravinski (1990b) was run, even though our FM-BEM formulation is based on the full-space fundamental solutions whereas Mossessian & Dravinski (1990b) use the half-space fundamental solutions. The mesh sizes used in Sec. 5.3.5 remain relatively modest for the FMM, the main computational limitation being currently caused by large GMRES iteration counts at the higher sampling frequencies (up to $O(10^4)$ for this example). Clearly, the current lack of a preconditioning strategy in the present formulation must be addressed in the near future (see e.g. Alléon et al. 1997 or Carpentieri et al. 2005 for various preconditioning approaches for Maxwell FM-BEMs).

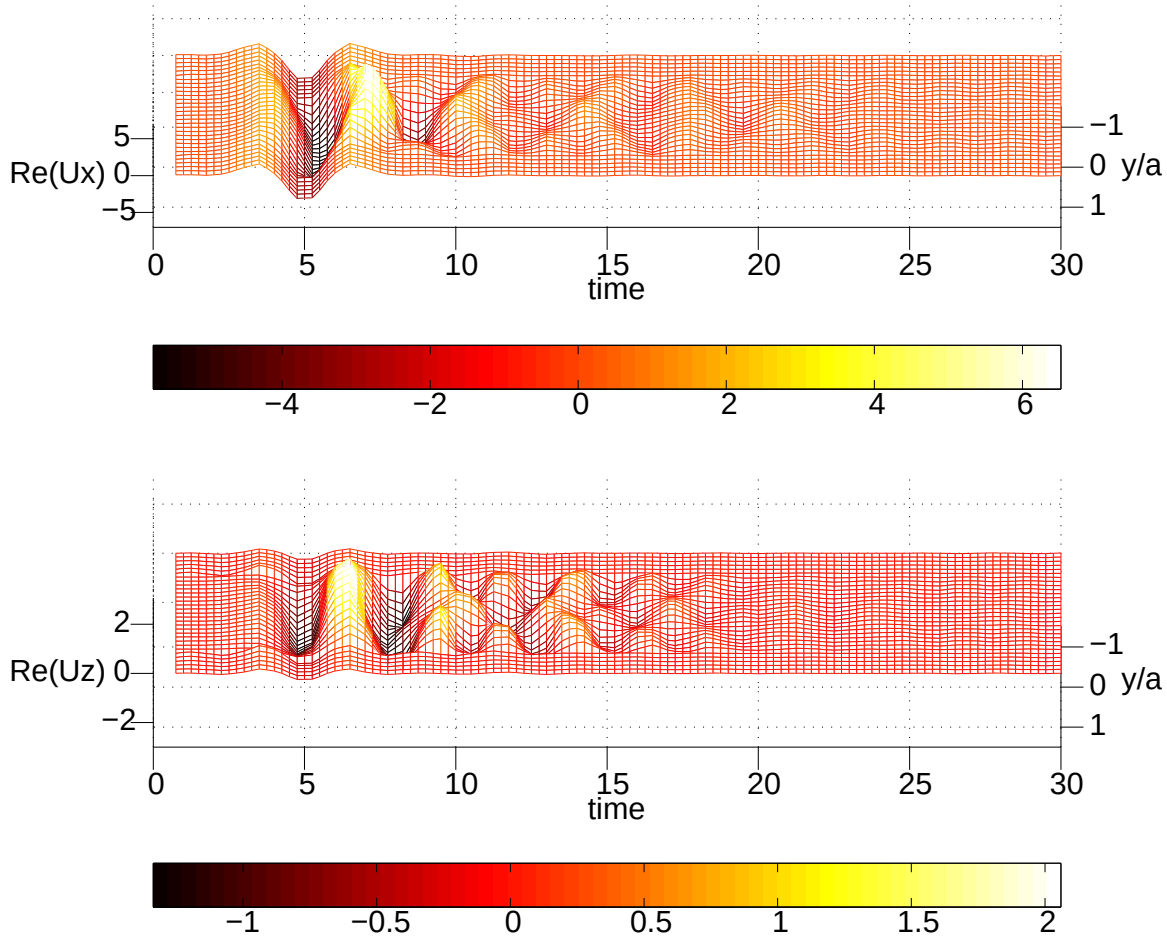

Figure 23. Propagation of an oblique ($\theta = 30°$) incident plane SV-wave in a semi-spherical alluvial basin, $f_0 = 0.25$Hz: x- (top) and z-components (bottom) of FMM computed displacement along the Oy axis against time.

6 CONCLUSIONS

In this article, a multi-level multi-domain fast multipole formulation has been proposed, based on previous works on single-region FMM (Chaillat et al. 2008). A BE-BE coupling strategy has been presented. Comparisons with the analytical or previously published numerical results show the efficiency and accuracy of the present implementation.

The analysis of seismic wave propagation in canonical basins, for higher frequencies than in previously published results, show the numerical efficiency of the method and suggest that it is suitable to deal with realistic seismological applications. The transient response of 3-D basins has also been investigated to illustrate the large domain of application of the method.

We have seen that the method is now limited by the iteration counts and so that a preconditioning strategy needs to be introduced. Moreover, for time domain response, the code is already competitive with time domain methods but will be more efficient when the half-space fundamental solutions will be used. Ongoing work deals with the formulation of multipole expansions of the half-space fundamental solutions.

Moreover, because the hypothesis of a linear elastic medium is often not sufficient, ongoing work also deals with the FMM formulation in attenuating media.

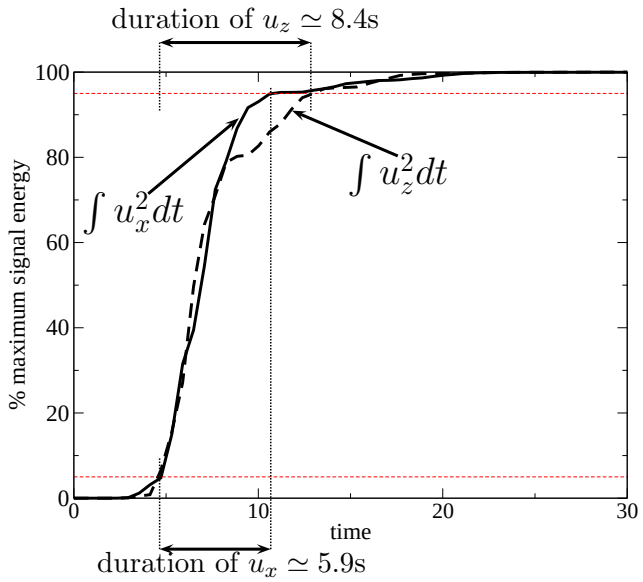

Figure 24. Estimation of the signal duration for the x- and z-components of displacement at the basin center, $f_0 = 0.25$Hz.

ACKNOWLEDGMENTS

This work is part of the project Quantitative Seismic Hazard Assessment (QSHA) funded by the French National Research Agency (ANR, http://qsha.unice.fr/). The authors thank Adrien Loseille from Gamma team, INRIA Rocquencourt for his help to create the meshes used in this article and Elise Delavaud from Potsdam University for providing us her numerical results.

APPENDIX A: ANALYTICAL SOLUTION OF THE TEST PROBLEM OF A PRESSURIZED CAVITY ENCLOSED IN A SPHERE

The analytical solution of the test problem (Section 4.2.1) can be easily computed. The potentials ϕ_i, defined such that $u_i = \partial\phi_i/\partial r$, can be written:

$$\begin{aligned} \phi_1 = &\quad \frac{A_1}{r} e^{ik_P^{(1)} r} + \frac{B_1}{r} e^{-ik_P^{(1)} r} \\ \phi_2 = &\quad \frac{A_2}{r} e^{ik_P^{(2)} r} \end{aligned} \tag{A.1}$$

where $k_P^{(i)}$ denote the P wavenumber in the subdomain i and the coefficients A_1, B_1 and A_2 are the solutions of the linear system:

$$\begin{bmatrix} e^{\alpha_1}(-1+\alpha_1) & -e^{-\alpha_1}(1+\alpha_1) & -e^{\alpha_2} \\ e^{\alpha_1}\mu_1\theta_1 & e^{-\alpha_1}\mu_1(\frac{\alpha_1^2}{\gamma_1^2}+4(1+\alpha_1)) & e^{\alpha_2}\mu_2\theta_2 \\ e^{\alpha_3}\mu_1\theta_3 & e^{-\alpha_3}\mu_1(\frac{\alpha_3^2}{\gamma_1^2}+4(1+\alpha_3)) & 0 \end{bmatrix} \times \begin{bmatrix} A_1 \\ B_1 \\ A_2 \end{bmatrix} = \begin{bmatrix} 0 \\ 0 \\ -pa_1^3 \end{bmatrix} \tag{A.2}$$

with $\alpha_1 = ik_P^{(1)} a_2$, $\alpha_2 = ik_P^{(2)} a_2$, $\alpha_3 = ik_P^{(1)} a_1$ and $\theta_i = \frac{\alpha_i^2}{\gamma_i^2} + 4(1-\alpha_i)$.

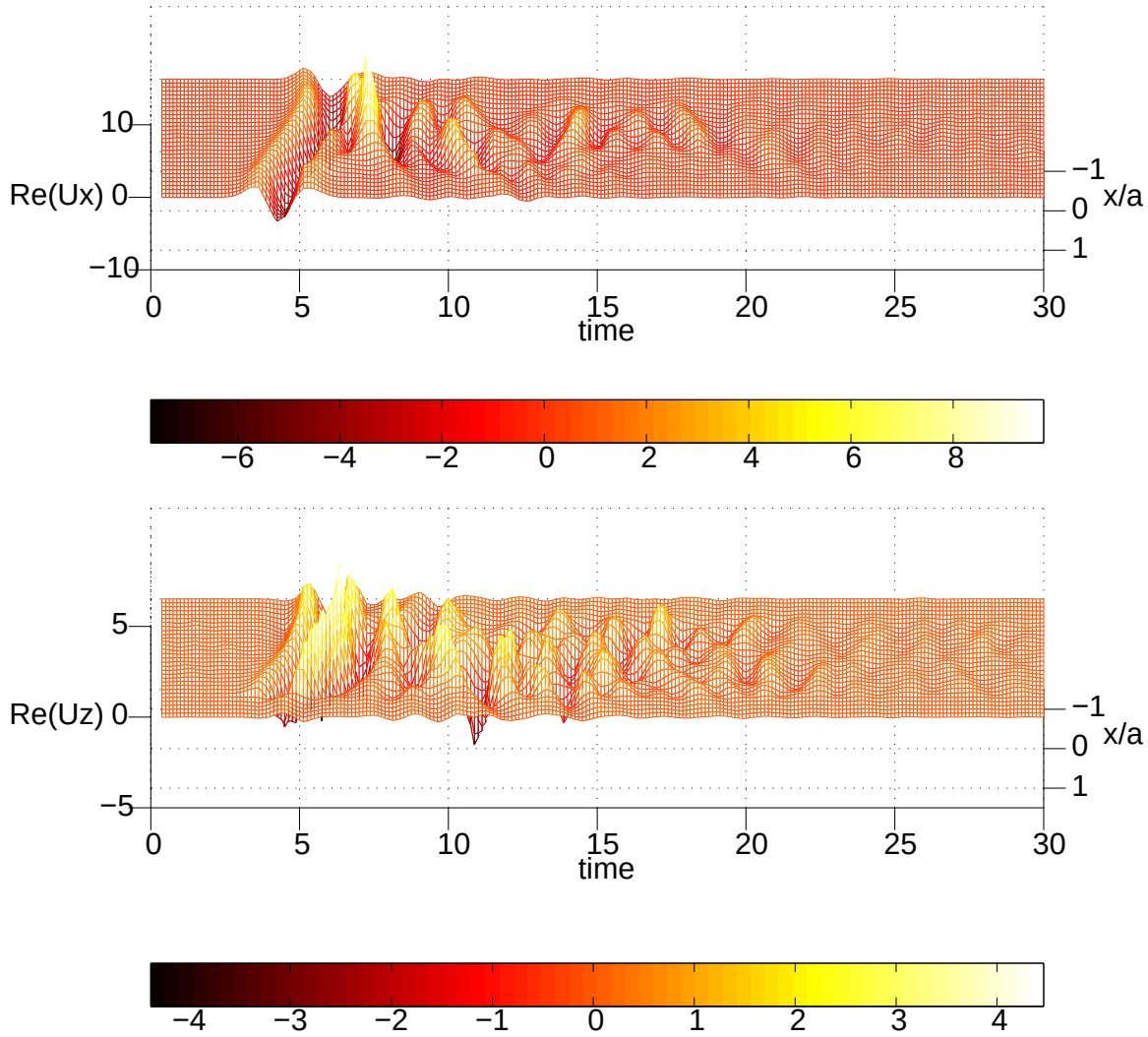

Figure 25. Propagation of an oblique ($\theta = 30°$) incident plane SV-wave in a semi-spherical alluvial basin, $f_0 = 0.5$Hz: x- (top) and z-components (bottom) of the FMM computed displacement on the Ox axis against time.

REFERENCES

Alléon, G., Benzi, M., & Giraud, L., 1997. Sparse approximation inverse preconditioning for dense linear systems arising in computational electromagnetics., *Numer. Algor.*, **16**, 1–15.

Araújo, F. C., Martins, C. J., & Mansur, W. J., 2001. An efficient BE iterative-solver-based substructuring algorithm for 3-D time-harmonic problems in elastodynamics, *Eng. Analysis with Boundary Elements*, **25**, 795–803.

Bard, P. Y. & Bouchon, M., 1985. The 2D resonance of sediment-filled valleys., *Bull. seism. Soc. Am.*, **75**, 519–541.

Bielak, J., Loukakis, K., Hisada, Y., & Yoshimura, C., 2003. Domain Reduction Method for Three-Dimensional Earthquake Modeling in Localized Regions, Part I: Theory, *Bull. seism. Soc. Am.*, **93**, 817–824.

Bielak, J., Ghattas, O., & Kim, E. J., 2005. Parallel octree-based finite element method for large-scale earthquake ground motion simulation, *Computer modeling in engineering and science*, **10**, 99–112.

Bonnet, M., 1999. *Boundary Integral Equation Method for Solids and Fluids*, Wiley.

Bouchon, M., Schultz, C. A., & Toksoz, M. M., 1995. A fast implementation of boundary integral

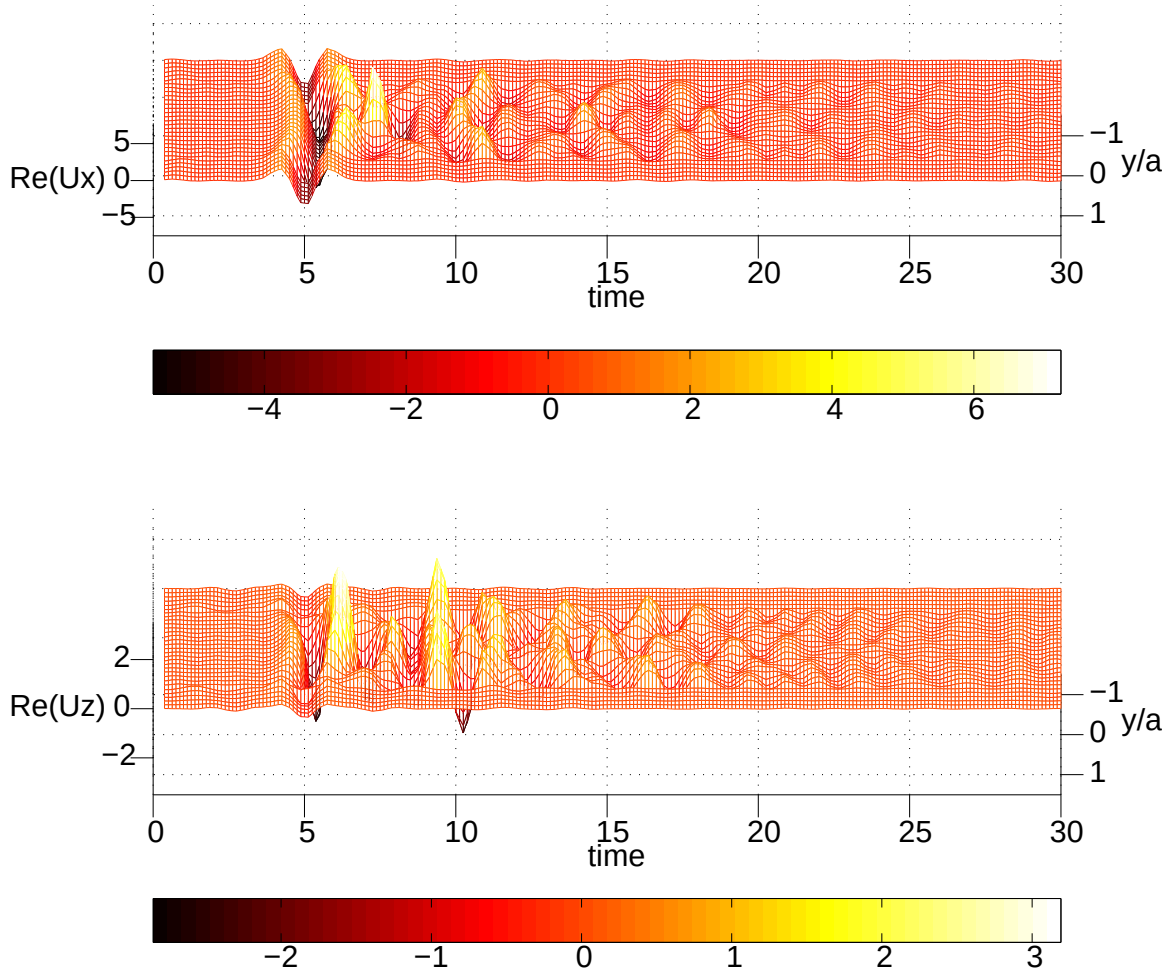

Figure 26. Propagation of an oblique ($\theta = 30°$) incident plane SV-wave in a semi-spherical alluvial basin, $f_0 = 0.5$Hz: x- (top) and z-components (bottom) of the FMM computed displacement on the Oy axis against time.

equation methods to calculate the propagation of seismic waves in laterally varying layered media, *Bull. seism. Soc. Am.*, **85**, 1679–1687.

Bui, H. D., Loret, B., & Bonnet, M., 1985. Régularisation des équations intégrales de l'élastostatique et de l'élastodynamique, *C.R. Acad. Sci. Paris, série II*, **300**, 633–636, in French.

Çakir, Ö., 2006. The multilevel fast multipole method for forward modelling the multiply scattered seismic surface waves, *Geophys. J. Int.*, **167**, 663–678.

Carpentieri, B., Duff, I. S., & Giraud, L. abd Sylvand, G., 2005. Combining fast multipole techniques and an approximate inverse preconditioner for large electromagnetism calculations, *SIAM J. Sci. Comput.*, **27**, 774–792.

Chaillat, S., Bonnet, M., & Semblat, J. F., 2008. A multi-level fast multipole BEM for 3-D elastodynamics in the frequency domain, *Comput. Methods Appl. Mech. Engng.*, **197**, 4233–4249.

Dangla, P., Semblat, J. F., Xiao, H., & Delépine, N., 2005. A simple and efficient regularization method for 3D BEM : application to frequency-domain elastodynamics, *Bull. seism. Soc. Am.*, **95**, 1916–1927.

Darve, E., 2000. The fast multipole method: Numerical implementation, *J. Comp. Phys.*, **160**, 195–240.

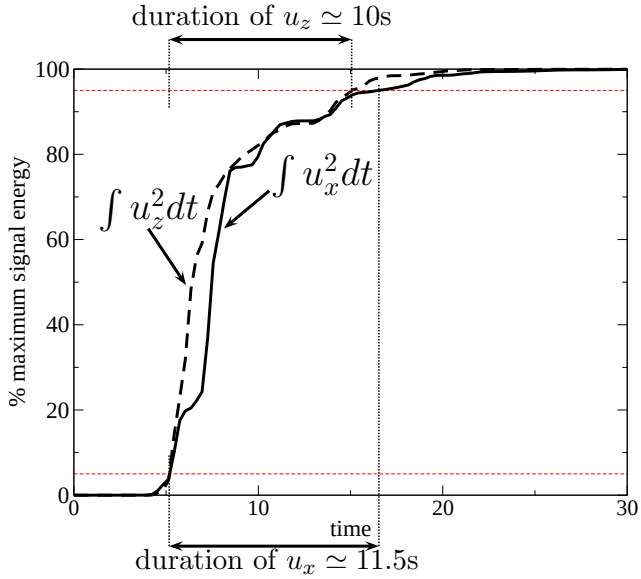

Figure 27. Estimation of the signal duration for the x- and z-components of displacement at the basin center, $f_0 = 0.50$Hz.

Darve, E. & Havé, P., 2004. A fast multipole method for maxwell equations stable at all frequencies., *Phil. Trans. Roy. Soc. (London)*, **A362**, 603–628.

Delavaud, E., 2007. *Simulation numérique de la propagation d'ondes en milieu géologique complexe: application à l'évaluation de la réponse sismique du bassin de Caracas (Venezuela)*, Ph.D. thesis, Institut de Physique du Globe de Paris, in French, www.ipgp.jussieu.fr/ Delavaud/ThesisDelavaud.pdf.

Epton, M. A. & Dembart, B., 1995. Multipole translation theory for the three-dimensional Laplace and Helmholtz equations, *SIAM J. Sci. Comp.*, **16**, 865–897.

Eringen, A. C. & Suhubi, E. S., 1975. *Elastodynamics, II-linear theory*, Academic Press.

Faccioli, E., Maggio, F., Paolucci, R., & Quarteroni, A., 1997. 2D and 3D elastic wave propagation by a pseudo-spectral domain decomposition method, *J. Seismology*, **1**, 237–251.

Frankel, A. & Vidale, J., 1992. A Three-Dimensional Simulation of Seismic Waves in the Santa Clara Valley, California, from a Loma Prieta Aftershock, *Bull. seism. Soc. Am.*, **82**, 2045–2074.

Fujiwara, H., 2000. The fast multipole method for solving integral equations of three-dimensional topography and basin problems, *Geophys. J. Int.*, **140**, 198–210.

Guiggiani, M. & Gigante, A., 1990. A general algorithm for multidimensional Cauchy principal value integrals in the boundary element method, *ASME J. Appl. Mech.*, **57**, 906–915.

Gumerov, N. A. & Duraiswami, R., 2005. *Fast multipole methods for the Helmholtz equation in three dimensions*, Elsevier.

Guzina, B. B. & Pak, R. Y. S., 2001. On the analysis of wave motions in a multi-layered solid, *Quart. J. Mech. Appl. Math.*, **54**, 13–37.

Hughes, T. J. R., Reali, A., & Sangalli, G., 2008. Duality and Unified Analysis of Discrete Approximations in Structural Dynamics and Wave Propagation: Comparison of p-method Finite Elements with k-method NURBS, *Computational Methods in Applied Mechanics and Engineering*, **197**, 4104–4124.

Ihlenburg, F. & Babuška, I., 1995. Dispersion analysis and error estimate of galerkin finite element methods for the Helmholtz equation, *Int. J. Numer. Meth. Engng.*, **38**, 3745–3774.

Komatitch, D. & Vilotte, J. P., 1998. The spectral element method: an efficient tool to simulate the seismic response of 2D and 3D geological structures, *Bull. seism. Soc. Am.*, **88**, 368–392.

Komatitsch, D., Liu, Q., Tromp, J., Süss, P., Stidham, C., & Shaw, J. H., 2004. Simulations of Ground Motion in the Los Angeles Basin based upon the Spectral-Element Method, *Bull. seism. Soc. Am.*, **94**, 187–206.

Krishnasamy, G., Rizzo, F. J., & Rudolphi, T. J., 1992. *Hypersingular boundary integral equations: their occurrence, interpretation, regularization and computation*, Developments in Boundary Ele-

ment Methods, Elsevier.

Kupradze, V. D., 1963. *Dynamical problems in elasticity*, vol. 3 of **Progress in solids mechanics**, North Holland.

Lee, V. W., 1984. 3D diffraction of plane P-, SV- and SH-waves by a hemispherical alluvial valley., *Soil. Dyn. Earthquake Engng.*, **3**, 133–144.

Lu, C. C. & Chew, W. C., 1994. A multilevel algorithm for solving a boundary integral equation of wave scattering., *Microwave Opt. Technol. Lett.*, **7**, 466–470.

Madyarov, A. I. & Guzina, B. B., 2006. A radiation condition for layered elastic media, *J. Elasticity*, **82**, 73–98.

Makra, K., Chavez-Garcia, F. J., Raptakis, D., & Pitilakis, K., 2005. Parametric analysis of the seismic response of a 2D sedimentary valley: implications for code implementations of complex site effects, *Soil Dynamics and Earthquake Engineering*, **25**, 303–315.

Moczo, P., Kristek, J., Galis, M., Pazak, P., & Balazovjech, M., 2007. The finite-difference and finite-element modeling of seismic wave propagation and earthquake motion, *Acta physica slovaca*, **57**, 177–406.

Mossessian, T. K. & Dravinski, M., 1990a. Amplification of elastic waves by a three dimensional valley. part 2: Transient response, *Earthquake Engng. Struct. Dyn.*, **19**, 681–691.

Mossessian, T. K. & Dravinski, M., 1990b. Amplification of elastic waves by a three dimensional valley. part 1: Steady state response, *Earthquake Engng. Struct. Dyn.*, **19**, 667–680.

Nishimura, N., 2002. Fast multipole accelerated boundary integral equation methods, *Appl. Mech. Rev.*, **55**, 299–324.

Niu, Y. & Dravinski, M., 2003. Direct 3D BEM for scattering of elastic waves in a homogenous anisotropic half-space, *Wave Motion*, **38**, 165–175.

Ortiz-Alemán, C., Sánchez-Sesma, F. J., Rodríguez-Zúniga, J. L., & Luzón, F., 1998. Computing topographical 3-D site effects using a fast IBEM/conjugate gradient approach, *Bull. seism. Soc. Am.*, **88**, 393–399.

Pak, R. Y. S. & Guzina, B. B., 1999. Seismic soil-structure interaction analysis by direct boundary element methods, *Int. J. Solids Struct.*, **36**, 4743–476.

Paolucci, R., 1999. Shear resonance frequencies of alluvial valleys by Rayleigh's method, *Earthquake Spectra*, **15**, 503–521.

Paolucci, R., 2002. Amplification of earthquake ground motion by steep topographic irregularities, *Earthquake Eng. and Structural Dynamics*, **31**, 1831–1853.

Pecker, A., 2005. Maximum ground surface motion in probabilistic seismic hazard analyses, *J. Earthquake Eng.*, **9**, 187–211.

Saad, Y. & Schultz, M. H., 1986. Gmres - a generalized minimal residual algorithm for solving nonsymmetric linear-systems, *SIAM J. Sci. Statist. Comput.*, **7**, 856–869.

Saenger, E. H., . Gold, N., & Shapiro, S. A., 2000. Modeling the propagation of elastic waves using a modified finite-difference grid, *Wave Motion*, **31**, 77–92.

Sánchez-Sesma, F. J., 1983. Diffraction of elastic waves by 3D surface irregularities, *Bull. seism. Soc. Am.*, **73**, 1621–1636.

Sánchez-Sesma, F. J. & Luzón, F., 1995. Seismic Response of Three-Dimensional Alluvial Valleys for Incident P, S and Rayleigh Waves, *Bull. seism. Soc. Am.*, **85**, 269–284.

Semblat, J. F., Paolucci, R., & Duval, A. M., 2003. Simplified vibratory characterization of alluvial basins., *C. R. Geoscience*, **335**, 365–370.

Semblat, J. F., Kham, M., Parara, E., Bard, P. Y., Makra, K., & Raptakis, D., 2005. Site effects: basin geometry vs soil layering., *Soil. Dyn. Earthquake Engng.*, **25**, 529–538.

Sylvand, G., 2002. *La méthode multipôle rapide en éléctromagnétisme : performances, parallélisation, applications*, Ph.D. thesis, ENPC, in French, http://pastel.paristech.org/308/.

Takahashi, T., Nishimura, N., & Kobayashi, S., 2003. A fast BIEM for three-dimensional elastodynamics in time domain, *Eng. Analysis with Boundary Elements*, **27**, 491–506.

Trifunac, M. D. & Brady, A. G., 1975. A study on the duration of strong earthquake ground motion, *Bull. seism. Soc. Am.*, **65**, 581–625.